Electronic Supplementary Material (ESI) for ChemComm.
This journal is © The Royal Society of Chemistry 2021

Supporting Information

Probing optical and magnetic properties via subtle stereoelectronic effects in mononuclear Dy^{III}-complexes

Alexandros A. Kitos,[a] Diogo A. Gálico,[a] Niki Mavragani,[a] Raúl Castañeda,[a] Jani O. Moilanen,*[b] Jaclyn L. Brusso*[a] and Muralee Murugesu*[a]

Table of Contents:

Experimental Section	**S2**
Single-crystal X-ray crystallography	**S2-S3**
Molecular, Theoretical and Supramolecular features of complexes 1 and 2	**S3-S15**
Magnetic Measurements	**S15-S30**
Theoretical Studies	**S31-S40**
Luminescent Studies	**S41**
Thermometry	**S42-S44**
References	**S45-S47**

[a]*Department of Chemistry and Biomolecular Sciences, University of Ottawa, 10 Marie Curie, Ottawa, Ontario, K1N 6N5, Canada.*
[b] *Department of Chemistry, Nanoscience Centre, University of Jyväskylä, P.O. Box 35, FI-40014, Finland*
E-mail: jani.o.moilanen@jyu.fi, jbrusso@uottawa.ca and m.murugesu@uottawa.ca

EXPERIMENTAL SECTION

Materials and physical measurements. The starting material *N*-2-pyridylimidoyl-2-pyridylamidine (Py_2ImAm) and pyrimidine-2-carboximidamide (PmAm) were synthesized as described in the literature.[1,2] Complex [Dy(acac)$_3$(PyAm)] (**1**) was synthesized following a recent synthetic procedure published by our group.[3] All the other chemicals purchased, were of reagent grade and used without further purification. FT-IR spectra (4000-400 cm^{-1}) were recorded using a Nicolet 6700 FT-IR spectrometer.

Preparation of [Dy(acac)$_3$(PyAm)] (1). Solid Dy(acac)$_3$·2H_2O (0.050 g, 0.10 mmol) was added to a pale yellow solution of Py_2ImAm (0.023 g, 0.10 mmol) in MeOH (10 mL). The resultant yellow solution was stirred for 2 hours, filtered and the filtrate was left undisturbed to evaporate. After a period of 4–5 days, colorless needle-like crystals were formed and collected by filtration, washed with Et_2O (2x1 mL) and dried in air. Yield = 34%. Analytical data, calcd for $C_{21}H_{28}N_3O_6Dy$ (found values are in parentheses): C 43.41 (43.02), H 4.86 (4.90), N 7.23 (7.21)%.

Preparation of [Dy(acac)$_3$(PmAm)] (2). This complex was prepared in an identical manner to **1** by simply replacing the Py_2ImAm ligand with the equivalent amount of PmAm ligand. Typical yields were in the 30% to 40% range. Analytical data, calcd for $C_{20}H_{27}N_4O_6Dy$ (found values are in parentheses): C 41.28 (41.11), H 4.68 (4.39), N 9.63 (9.60)%.

Single-crystal X-ray crystallography. Crystals of **2** suitable for single-crystal X-ray diffraction (SCXRD) analysis were covered in parabar oil and mounted on a thin glass fiber. Diffraction data (ω- and ϕ-scans) were collected on a Bruker AXS SMART single-crystal diffractometer at 200 K using Mo-Kα radiation (λ = 0.71073 Å). The reflection intensities were corrected for absorption by using multi-scan of the SADABS[4] program. The structure was solved using direct methods with SHELXT[5] and refined by the full-matrix least-squares methods on F^2 with SHELXL-2018/3.[6] Carbon-bound hydrogen atoms were included and refined in calculated positions (riding model), while imino N-H and amino N-H_2 hydrogen atoms of the PmAm ligand were located in difference Fourier maps and refined isotropically. All geometric/crystallographic calculations were carried out using SHAPE,[7] PLATON[8], Crystal Explorer[9] and WINGX[10] programs while graphics were prepared with DIAMOND[11] and MERCURY.[12] The crystallographic data and structure refinement summary for complex **2** are listed in Table S1. For comparison reasons, the crystallographic data of **1** are also included in Table S1.

Table S1: Crystallographic data for compounds **1**[3] and **2**.

Compound reference	**1**[3]	**2**
Chemical formula	$C_{21}H_{28}DyN_3O_6$	$C_{20}H_{27}DyN_4O_6$
Formula mass	580.96	581.95
Crystal system	Monoclinic	Monoclinic
a/Å	16.8883(16)	9.8270(9)
b/Å	8.3030(8)	12.6308(10)
c/Å	17.7708	19.5062(18)
α/°	90	90
β/°	106.605	100.309(3)
γ/°	90	90
Unit cell volume/Å^3	2388.0(4)	2382.1(4)
Temperature/K	200(2)	200(2)
Space group	$P2_1/n$	$P2_1/c$
No. of formula units/unit cell, *Z*	4	4
Radiation type	Mo Kα	Mo Kα
Absorption coefficient, μ/mm^{-1}	3.168	3.177
No. of reflections measured	36627	39480
No. of independent reflections	5216	4676
R_{int}	0.0901	0.0635
Final R_1values (I> 2σ(I))	0.0361	0.0300
Final $wR_2(F^2)$ values (I> 2σ(I))	0.0661	0.0633
Final R_1 values (all data)	0.0623	0.0436
Final $wR_2(F^2)$ values (all data)	0.0747	0.0697
Goodness of fit on F^2	1.033	1.044
CCDC number	2004822	2081829

Molecular and Supramolecular features of complexes 1 and 2.

Single-crystal X-ray diffraction analysis reveals that **1** and **2** crystallize at the monoclinic $P2_1$/n and $P2_1$/c space groups, respectively. The Dy(III) ions in both structures are coordinated to one PyAm or PmAm ligand, which act as *N-N* bidentate chelates through the pyridyl or pyrimidyl N1 and amidic N2 atoms. The coordination environment around the Dy(III) centers is completed by three bidentate chelating acetylacetonato groups, leading to an eight coordinate DyO_6N_2 environment. The analysis using the method of Continuous Shape Measures (CShMs) gives a deviation parameter *P* of 0.484 and 0.503 (Table S2) for D_{2d} and D_{4d} symmetry Dy(III) ions in **1** and **2**, which correspond to a triangular dodecahedron and square antiprismatic geometry, respectively. All Dy-O/Dy-N bond distances (Table S4) are typical for 8-coordinate Dy(III) complexes. Comparisons of the molecular overlay of **1** and **2**, along with their unit cell parameters (Table S3), clearly confirm the different rearrangement of the ligands around the metal centers. Based on the IR spectra, no significant differences were observed due to the similar ligation of both complexes.

Table S2. Results from Shape analysis for both complexes.

Complex	Label	Shape	Symmetry	CShM
[Dy(acac)$_3$(PyAm)]	SAPR-8	Square antiprism	D_{4d}	1.85348
	TDD-8	**Triangular dodecahedron**	**D_{2d}**	**0.48446**
[Dy(acac)$_3$(PmAm)]	**SAPR-8**	**Square antiprism**	**D_{4d}**	**0.50378**
	TDD-8	Triangular dodecahedron	D_{2d}	2.08996

Table S3. Comparison of the unit cell parameters of **[Dy(acac)$_3$(PyAm)]** and **[Dy(acac)$_3$(PmAm)]**.

Compound	a/Å	*b*/Å	*c*/Å	*α*/°	*β*/°	*γ*/°	V/Å^3	Space group	Reference
[Dy(acac)$_3$(PyAm)]	16.8883(16)	8.3030(8)	17.7708(17)	90	106.605(3)	90	2388.0(4)	$P2_1/n$	3
[Dy(acac)$_3$(PmAm)]	9.8270(9)	12.6308(10)	19.5062(18)	90	100.309(3)	90	2382.1(4)	$P2_1$/c	This work

Table S4. Selected interatomic distances (Å) for **[Dy(acac)$_3$(PyAm)]** and **[Dy(acac)$_3$(PmAm)]**.

[Dy(acac)$_3$(PyAm)]		[Dy(acac)$_3$(PmAm)]	
Dy-O4	2.309(3)	Dy-O4	2.313(3)
Dy-O5	2.314(3)	Dy-O5	2.327(3)
Dy-O3	2.328(3)	Dy-O3	2.357(3)
Dy-O1	2.341(3)	Dy-O1	2.322(3)
Dy-O6	2.371(3)	Dy-O6	2.331(3)
Dy-O2	2.384(3)	Dy-O2	2.351(3)
Dy-N2	2.447(4)	Dy-N2	2.453(3)
Dy-N1	2.608(4)	Dy-N1	2.614(3)

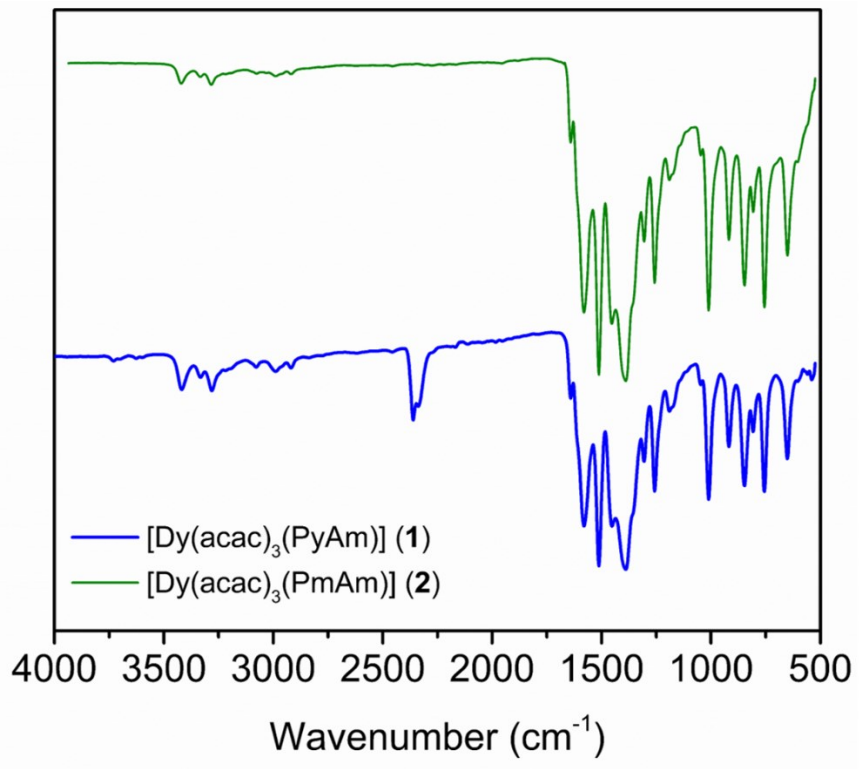

Figure S1. Comparison of the IR spectrum of **1** (blue) and **2** (green). Bands in the region of ~3450 – 3250 cm^{-1} are attributed to the *ν*(NH) vibration of the coordinated amidine ligands and the bands at 1640 cm^{-1} can be assigned to the *ν*(C=N) stretching vibration of the PyAm or PmAm ligands. The strong absorption peaks between ~1600 – 1380 cm^{-1} can be attributable to the C=C and C=O stretching modes of acac$^-$.[13]

Strong (N-H···O) and weak (C-H···O) hydrogen bonds are present in the crystal packing of both complexes (Table S5). In complex **1** neighbouring mononuclear molecules interact through strong H-bonds (N2-H2A···O2 and N3-H3A···O6) to form "dimeric" units (Figure S2); these units form chains along the *b* axis *via* N3-H3B···O6 H-bonds. The structure is further stabilized *via* weak C17-H17···O5 H-bonds, forming a 2-D supramolecular network. In contrast, neighboring [Dy(acac)$_3$(PmAm)] (**2**) molecules are forming chains along the *b* axis through strong N2-H2A···O1, N2-H2A···O5, N3-H3A···O3 and weak C16-H16···O2 hydrogen bonds (Figure S2). The imino hydrogen H2A is participating in two strong H-bonds at the same time leading to the formation of bifurcated hydrogen bonds with an overall angle around the H2A close to 360°. Despite the presence of the pyridyl or pyrimidine aromatic rings in the crystal structures of **1** and **2** no π···π stacking or C-H···π interactions were observed. The closest Dy^{III}···Dy^{III} distances within the chains are 8.303(9) and 6.659(6) Å for complex **1** and **2** respectively.

Table S5. Geometry (Å, °) of the hydrogen bonds that are present in both complexes.

[Dy(acac)$_3$(PyAm)]					
N2-H2A···O6	0.86(4)	2.44(4)	3.141(5)	141(4)	1-x, 1-y, 1-z
N3-H3A···O2	0.88(5)	2.50 (5)	3.195 (6)	137(4)	1-x, 1-y, 1-z
N3-H3A···O6	0.88(5)	2.59(5)	3.252(6)	133(4)	1-x, 1-y, 1-z
N3-H3B···O2	0.88(5)	2.27(4)	3.121(5)	162(5)	x, -1+y, z
C17-H17···O1	0.95	2.639	3.582(9)	172	3/2-x, 1/2+y, 1/2-z
[Dy(acac)$_3$(PmAm)]					
N2-H2A···O1	0.86(2)	2.39(3)	3.146(5)	147(4)	1-x, 1/2+y, 1/2-z
N2-H2A···O5	0.86(2)	2.49(5)	3.131(5)	132(5)	1-x, 1/2+y, 1/2-z
N3-H3A···O3	0.86(3)	2.39(3)	3.192(5)	155(5)	1-x, 1/2+y, 1/2-z
C16-H16···O2	0.95	2.56	3.310(5)	136	1-x, -1/2+y, 1/2-z

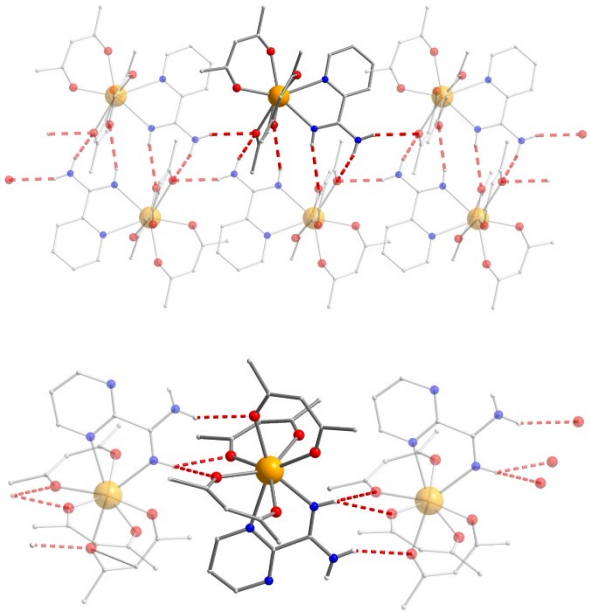

Figure S2. Part of the supramolecular arrangement of **[Dy(acac)$_3$(PyAm)]** (upper) and **[Dy(acac)$_3$(PmAm)]** (lower) illustrating the chains formed by strong N−H···O hydrogen-bonding (red dashed lines) along the *b* axis.

To characterize the degree of distortion of the square antiprism, all the relevant geometrical parameters such as the d_{pp}, the distance between the squares; d_{in}, the shorter atom distance in the square; Φ, the angle between the diagonals of the two squares (skew angle) and the angle between the tetragonal axis (*C4*) and the Ln–N,O vectors (α) were calculated. For the highest symmetry SAP, Φ is equal to 45° while α corresponds to the magic angle of 54.74° (Figure S3). Wider α angles correspond to compression and smaller to elongation along the *C4* axis. As shown in Figure S3 four oxygen atoms (O3, O4, O5 and O6) from two acac ligands compose an upper square and two oxygen atoms (O1 and O2) and two nitrogen atoms (N1 and N2) from one acac and one PmAm ligands, respectively, compose the lower square of SAP. Each square is twisted with respect to the other with the Φ angle being equal to 42.97° (Table S6). This angle is very close to that expected for an ideal D_{4d} symmetry (Φ = 45°). The average distance between the four neighboring atoms in the squares d_{in} is 2.815 Å and the interplanar distance (d_{pp}) is 2.617 Å between the upper and lower planes. The two planes are in a nearly parallel arrangement with a slight tilt angle of 1.55°. The ratio d_{in}/d_{pp} (1.076) is indicative of an axial distortion and along with the wider α angle found (56.67° versus the 54.74° of the ideal SAP; Table S7) is indicative of a compression of the square antiprism around the Dy(III) ion.

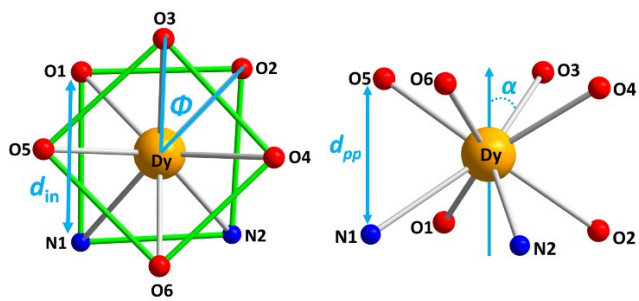

Figure S3. Definition of the relevant geometrical parameters in a square antiprism. Left (view along the tetragonal axis): d_{in}, the shorter atom distance in the square and Φ, the skew angle between the diagonals of the two squares. Right (lateral view, perpendicular to the axis which is represented by the light blue arrow): d_{pp}, the distance between the two parallel squares and α, the angle between the axis and the Ln–N,O vectors.

Table S6. Relevant structural parameters in square antiprismatic geometry, Φ angle.

Φ angle (°)	[Dy(acac)$_3$(PmAm)]
O1-Ln-O3	40.60
O3-Ln-O2	43.14
O2-Ln-O4	41.48
O4-Ln-N2	45.23
N2-Ln-O6	45.60
O6-Ln-N1	40.68
N1-Ln-O5	44.33
O5-Ln-O1	42.69
Deviation	**42.97**
Sum of deviation to ideal (45°)	**2.03**

Table S7. Relevant structural parameters in square antiprismatic geometry, *α* angle.

α angle (º)	[Dy(acac)$_3$(PmAm)]
O1	58.67
O2	60.92
N1	54.79
N2	52.40
O3	53.22
O4	57.15
O5	58.41
O6	57.80
Deviation	**56.67**
Sum of deviation to ideal (54.74º)	**1.93**

The supramolecular interactions in **[Dy(acac)$_3$(PyAm)] (1)** and **[Dy(acac)$_3$(PmAm)] (2)** are further discussed using the Hirshfeld Surface (HS) analysis and 2D fingerprint plot (FP) tools. The HS mapped with the d_{norm} and shape index, *S*, for both complexes are presented in Figure S4. The vivid red regions on the d_{norm} surfaces represent the significant N-H···O and C-H···O interactions, while the blue and white regions correspond to the H···H and C···H interactions. When the shape index function is applied to the HS, no"bow-tie"patterns or red/blue triangles observed indicating the complete absence of π···π stacking interactions.

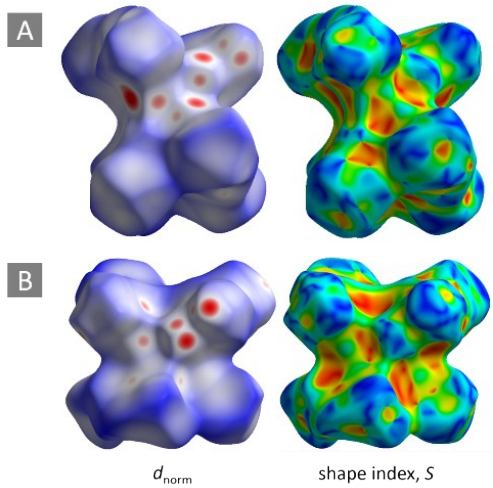

Figure S4. Hirshfeld surface (HS) for **[Dy(acac)$_3$(PyAm)]** (A) and **[Dy(acac)$_3$(PmAm)]** (B) mapped over d_{norm} (left) and shape index, *S*, (right). In the d_{norm} HS a red–blue–white colour scheme used where red regions represent closer contacts, blue regions represent longer contacts and white regions represent the distance of contacts which is exactly equal to the *vdW* separation.

The FPs of **1** and **2** with all types of contributions in the HS are shown in Figure S5 (left) along with the FP plots for each different type of interaction (right). The spikes A and A´ in the plot are associated with the X-H···O (where X = C, N) hydrogen bonds while the "wings" B and B´ are associated with the C···H interactions. Finally, the sharp peak C is associated with the H···H interactions that further stabilize the supramolecular architectures of **1** and **2**. Additionally, FP analysis can be quantitative giving the values of the percentages of all the kinds of interactions present in the structures. In Figure S6 are summarized all the interactions along with their total contribution as percentages in the HS for **1** and **2**.

The values of the percentages for the X-H···O (where X = C, N) are 14.8 and 12.5% in complexes **1** and **2**, respectively, while the percentages of C···H are 13.0 and 19.0%, respectively. The C···C percentages are close to zero (1.5 and 0.1%) confirming the complete absence of π···π stacking in both structures. In complexes **1** and **2** the main intermolecular contacts are H···H interactions with the values of the percentages being more than 60% (Figure S6).

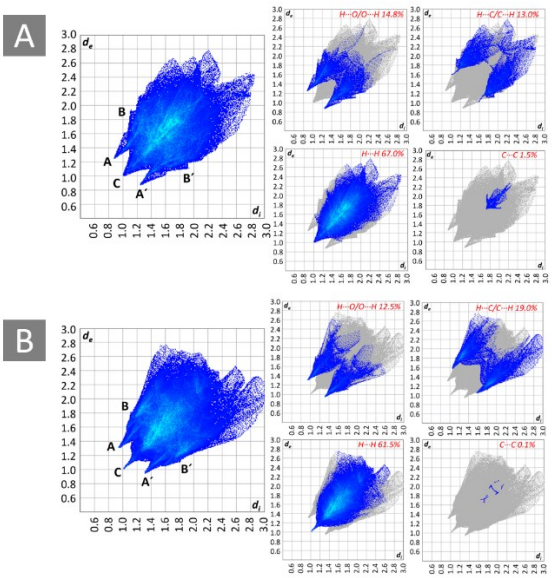

Figure S5. 2D fingerprint plots for all types of interactions along with their corresponding percentages in the crystal structures of **1** (A) and **2** (B).

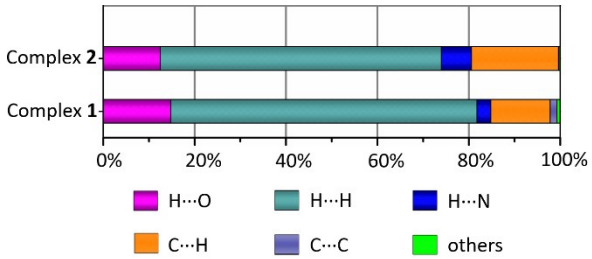

Figure S6. Relative contributions in percentage of all the intermolecular interactions to the Hirshfeld surface areas of complexes **1** and **2**.

Table S8: Calculated AIM charges for the selected atoms of **PyAm**, **PmAm**, **1**, and **2** at the PBE1PBE-D3/TZVP and PBE1PBE/TZVP levels of theory.

	PyAM		1			PmAm		2	
Atom	**PBE1PBE-D3**	**PBE1PBE**	**PBE1PBE-D3**	**PBE1PBE**	**Atom**	**PBE1PBE-D3**	**PBE1PBE**	**PBE1PBE-D3**	**PBE1PBE**
C16	0.53	0.53	0.54	0.54	**C16**	0.55	0.55	0.55	0.55
C17	-0.04	-0.04	-0.03	-0.03	**C17**	-0.05	-0.05	-0.03	-0.03
C18	-0.02	-0.02	-0.01	-0.01	**C18**	0.54	0.54	0.53	0.53
C19	-0.04	-0.04	-0.03	-0.03	**C19**	1.04	1.04	1.07	1.07
C20	0.52	0.52	0.52	0.52	**C20**	1.15	1.15	1.21	1.21
C21	1.13	1.13	1.16	1.16	**N1**	-1.11	-1.11	-1.19	-1.19
N1	-1.12	-1.12	-1.18	-1.18	**N2**	-1.11	-1.11	-1.20	-1.20
N2	-1.12	-1.12	-1.21	-1.21	**N3**	-1.18	-1.18	-1.20	-1.20
N3	-1.14	-1.14	-1.16	-1.16	**N4**	-1.18	-1.18	-1.18	-1.18
O1	-	-	-1.22	-1.22	**O1**	-	-	-1.22	-1.22
O2	-	-	-1.21	-1.21	**O2**	-	-	-1.22	-1.22
O3	-	-	-1.22	-1.21	**O3**	-	-	-1.22	-1.22
O4	-	-	-1.21	-1.22	**O4**	-	-	-1.21	-1.21
O5	-	-	-1.22	-1.22	**O5**	-	-	-1.21	-1.22
O6	-	-	-1.21	-1.21	**O6**	-	-	-1.22	-1.22

Table S9: Calculated densities (***ρ(r)***), Laplacians ($\nabla^2\boldsymbol{\rho}(r)$), and delocalization indices (*DI*) for the selected bond critical points (BCP) observed at the gas-phase optimized structures of **PyAm** and **1** at the PBE1PBE-D3/TZVP and PBE1PBE/TZVP levels of theory.

	PyAm (PBE1PBE-D3)			PyAm (PBE1PBE)			1 (PBE1PBE-D3)			1 (PBE1PBE)		
	$\boldsymbol{\rho}(r)$	$\nabla^2\boldsymbol{\rho}(r)$	*DI*	$\boldsymbol{\rho}(r)$	$\nabla^2\boldsymbol{\rho}(r)$	*DI*	$\boldsymbol{\rho}(r)$	$\nabla^2\boldsymbol{\rho}(r)$	*DI*	$\boldsymbol{\rho}(r)$	$\nabla^2\boldsymbol{\rho}(r)$	*DI*
BCP (O5-H16)	-	-	-	-	-	-	0.017	0.065	0.059	0.016	0.062	0.058
BCP (Dy1-N1)	-	-	-	-	-	-	0.032	0.117	0.147	0.029	0.108	0.137
BCP (Dy1-N2)	-	-	-	-	-	-	0.042	0.154	0.201	0.041	0.151	0.198
BCP (Dy1-O1)	-	-	-	-	-	-	0.051	0.229	0.242	0.051	0.231	0.249
BCP (Dy1-O2)	-	-	-	-	-	-	0.055	0.250	0.266	0.051	0.228	0.238
BCP (Dy1-O3)	-	-	-	-	-	-	0.050	0.224	0.237	0.048	0.215	0.228
BCP (Dy1-O4)	-	-	-	-	-	-	0.056	0.255	0.271	0.057	0.257	0.277
BCP (Dy1-O5)	-	-	-	-	-	-	0.053	0.235	0.249	0.051	0.229	0.244
BCP (Dy1-O6)	-	-	-	-	-	-	0.047	0.212	0.218	0.049	0.218	0.229
BCP (O5-H16)	-	-	-	-	-	-	0.017	0.065	0.059	0.016	0.062	0.058

Table S10: Calculated densities (***ρ(r)***), Laplacians ($\nabla^2\rho(r)$), and delocalization indices (*DI*) for the selected bond critical points (BCP) observed at the gas-phase optimized structures of **PmAm** and **2** at the PBE1PBE-D3/TZVP and PBE1PBE/TZVP levels of theory.

	PmAm (PBE1PBE-D3)			PmAm (PBE1PBE)			2 (PBE1PBE-D3)			2 (PBE1PBE)		
	$\rho(r)$	$\nabla^2\rho(r)$	*DI*	$\rho(r)$	$\nabla^2\rho(r)$	*DI*	$\rho(r)$	$\nabla^2\rho(r)$	*DI*	$\rho(r)$	$\nabla^2\rho(r)$	*DI*
BCP (N4-H3)	0.022	0.095	0.050	0.022	0.095	0.050	0.019	0.088	0.067	0.019	0.088	0.067
BCP (O5-H16)	-	-	-	-	-	-	0.010	0.041	0.031	0.010	0.040	0.032
BCP (Dy1-N1)	-	-	-	-	-	-	0.031	0.119	0.140	0.030	0.114	0.135
BCP (Dy1-N2)	-	-	-	-	-	-	0.042	0.156	0.202	0.041	0.153	0.202
BCP (Dy1-O1)	-	-	-	-	-	-	0.051	0.229	0.240	0.050	0.224	0.237
BCP (Dy1-O2)	-	-	-	-	-	-	0.052	0.236	0.246	0.051	0.230	0.244
BCP (Dy1-O3)	-	-	-	-	-	-	0.058	0.260	0.278	0.057	0.258	0.278
BCP (Dy1-O4)	-	-	-	-	-	-	0.052	0.233	0.248	0.051	0.226	0.241
BCP (Dy1-O5)	-	-	-	-	-	-	0.049	0.225	0.233	0.049	0.220	0.232
BCP (Dy1-O6)	-	-	-	-	-	-	0.050	0.227	0.239	0.050	0.223	0.236

Table S11: PBE1PBE-D3/TZVP N-M and O-M (M = Y or Dy) bond energies per each coordination bond (***ΔE_{bond}*** (**N-M**) and ***ΔE_{bond}*** (**N-M**)) and total bond energies (***ΔE_{bond}*** (**X-M**)) associated to the coordination bonds of **1** and **2** as well as the PBE1PBE-D3/pob-TZVP lattice stabilization energy (***$\Delta E_{lattice}$***) per one molecule for the yttrium analog of **2**. All values are given in kJmol^{-1}. As seen from the Table S11, the bond energies of $\mathbf{1_Y}$ and $\mathbf{2_Y}$ are in very good agreement with the bond energies of **1** and **2**. Thus, the lattice stabilization energy calculated for $\mathbf{2_Y}$ should reflect well the lattice stabilization energy of **2**.

Complex	ΔE_{bond} (N-M)[a]	ΔE_{bond} (O-M)[b]	ΔE_{bond_total} (X-M)[a]	$\Delta E_{lattice}$
1	-55.695	-258.287	-1661.111	-
$\mathbf{1_Y}$	-53.473	-255.565	-1640.338	[d]
2	-56.635	-263.032	-1691.463	-
$\mathbf{2_Y}$	-55.616	-260.249	-1672.724	-1338.416

a) ΔE_{bond} (***N-M***) = (**E**(**1**) – {**E**([M(acac)$_3$])+**E**(PyAm)}}/2 For **1** and ΔE_{bond} (***N-M***) = (**E**(**2**) – {**E**([M(acac)$_3$])+**E**(PmAm)}}/2 for **2**.

b) ΔE_{bond} (***O-M***) = (**E**(**1**) – {**E**([M(PyAm)(acac)$_2$]$^+$)+**E**([acac]$^-$)}}/2 For **1** and ΔE_{bond} (***O-M***) = (**E**(**2**) – {**E**([M(PmAm)(acac)$_2$]$^+$)+**E**([acac]$^-$)}}/2 for **2**.

c) ΔE_{bond_total} = 2 × ΔE_{bond} (**N-M**) + 4 × ΔE_{bond} (**O-M**)

d) No lattice stabilization energy was calculated for **1** because the Crystal17 does not support the *P2$_1$/n* space group.

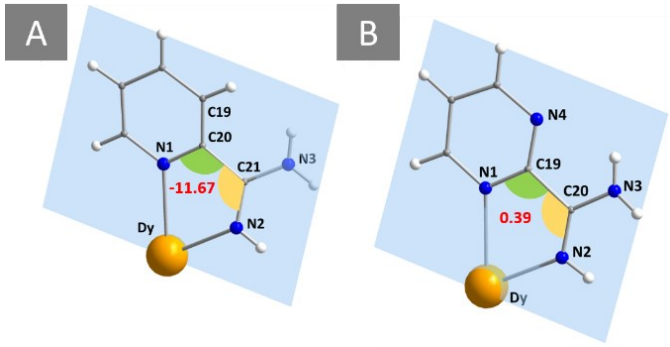

Figure S7. The N1-C20-C21-N2 dihedral angles of both ligands in **1** (A) and **2** (B) as discussed in the main text.

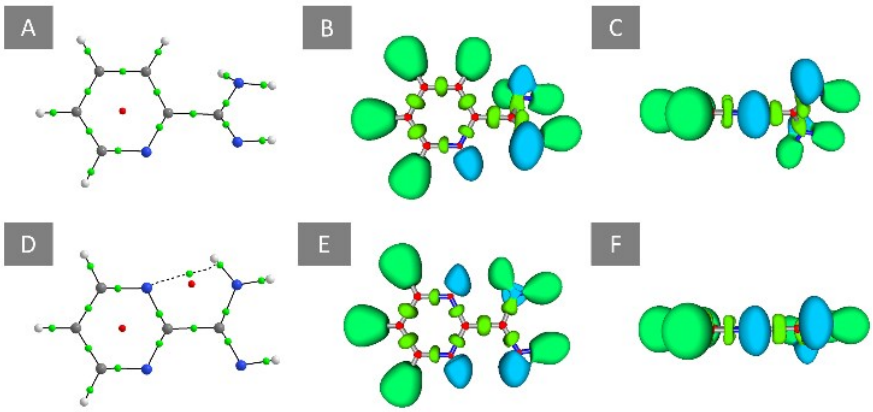

Figure S8. Bond baths (black lines), bond critical points (green spheres), and ring critical points (red spheres) for the gas-phase optimized structures of PyAm (a) and PmAm (d) as well as their ELF plots (η = 0.8) from two different perspective (b, c, e, and f). ELF basin colour code: red = core, green = bond, and blue = lone pair.

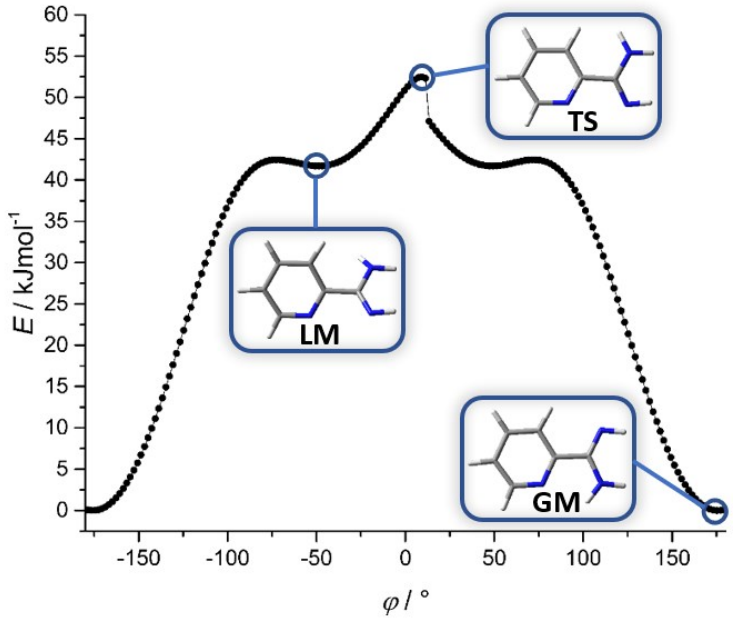

Figure S9. Potential energy surface as a function of dihedral angle N1-C20-C21-N2 (φ) for **PyAm** at the PBE1PBE-D3/TZVP level of theory. The molecular structure of the most important global (**GB**) minimum, local (**LM**) minimum and transition state (**TS**) are presented. Other global and local minima are mirror images of the presented ones, and in other two transition states - $C(NH)NH_2$ group has ~ 90° angle with the six-membered ring.

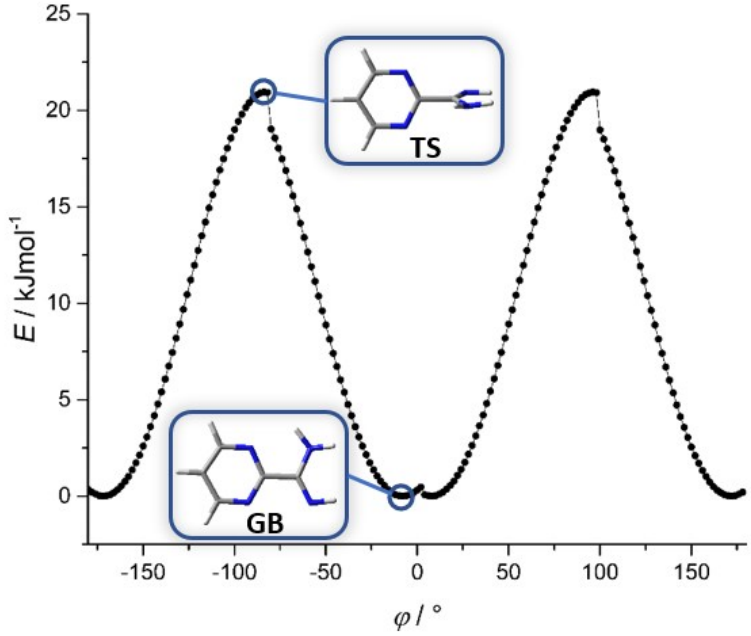

Figure S10. Potential energy surface as a function of dihedral angle N1-C19-C20-N2 (φ) for **PmAm** at the PBE1PBE-D3/TZVP level of theory. The most important molecular structures the global (**GB**) minimum and transition state (**TS**) are presented. Three other global minima can be generated from the presented one using the σ_h and/or C_2 symmetry operations. The two low

lying transition states correspond to the structures in which the -C(NH)NH_2 group is almost coplanar with the six membered ring.

Table S12: Selected bond lengths (*Å*), angles (°) and dihedral angles (°) for the gas-phase optimized structures of **PyAm** ligand and **1** at the PBE1PBE-D3/TZVP and PBE1PBE/TZVP levels of theory as well as their deviations from the experimental parameters (Exp-Calc) along with mean absolute errors (MAE).

		PBE1PBE-D3				PBE1PBE			
Bond	**Crystal**	**PyAm**	**Exp-Calc**	**1**	**Exp-Calc**	**PyAm**	**Exp-Calc**	**1**	**Exp-Calc**
N1-C16	1.338	1.327	0.011	1.326	0.012	1.327	0.011	1.326	0.012
C16-C17	1.376	1.389	-0.013	1.389	-0.013	1.389	-0.013	1.390	-0.014
C17-C18	1.376	1.385	-0.009	1.383	-0.007	1.385	-0.009	1.383	-0.007
C18-C19	1.371	1.385	-0.014	1.387	-0.016	1.386	-0.015	1.388	-0.017
C19-C20	1.374	1.393	-0.019	1.388	-0.014	1.394	-0.020	1.389	-0.015
C20-N1	1.343	1.331	0.012	1.333	0.010	1.331	0.012	1.334	0.009
C20-C21	1.484	1.497	-0.013	1.490	-0.006	1.498	-0.014	1.491	-0.007
C21-N2	1.290	1.269	0.021	1.275	0.015	1.270	0.020	1.275	0.015
C21-N3	1.344	1.382	-0.038	1.364	-0.020	1.382	-0.038	1.364	-0.020
Dy1-N1	2.607	-	-	2.644	-0.037	-	-	2.680	-0.073
Dy1-N2	2.446	-	-	2.510	-0.064	-	-	2.518	-0.072
Dy1-O1	2.341	-	-	2.356	-0.015	-	-	2.348	-0.007
Dy1-O2	2.383	-	-	2.317	0.066	-	-	2.357	0.026
Dy1-O3	2.328	-	-	2.364	-0.036	-	-	2.378	-0.050
Dy1-O4	2.309	-	-	2.309	0.000	-	-	2.306	0.003
Dy1-O5	2.315	-	-	2.340	-0.025	-	-	2.353	-0.038
Dy1-O6	2.371	-	-	2.387	-0.016	-	-	2.372	-0.001
MAE	**-**	**-**	**0.017**	**-**	**0.022**	**-**	**0.017**	**-**	**0.023**
Angle	**Crystal**	**PyAm**	**Exp-Calc**	**1**	**Exp-Calc**	**PyAm**	**Exp-Calc**	**1**	**Exp-Calc**
N1-Dy1-N2	62.83	-	-	61.67	1.16	-	-	60.81	2.02
O1-Dy1-O2	72.52	-	-	72.12	0.40	-	-	71.72	0.80
O3-Dy1-O4	73.93	-	-	72.89	1.04	-	-	72.43	1.50
O5-Dy1-O6	72.97	-	-	72.14	0.83	-	-	71.40	1.57
O1-Dy1-N1	75.48	-	-	69.02	6.46	-	-	71.41	4.07
O2-Dy1-N2	76.46	-	-	83.87	-7.41	-	-	77.89	-1.43
O1-Dy1-O3	73.52	-	-	77.62	-4.10	-	-	75.60	-2.08
O1-Dy1-O5	139.26	-	-	138.06	1.20	-	-	138.65	0.61
O2-Dy1-O4	79.39	-	-	82.99	-3.60	-	-	81.72	-2.33
O2-Dy1-O6	75.36	-	-	78.30	-2.94	-	-	77.09	-1.73
MAE	**-**	**-**	**-**	**-**	**2.91**	**-**	**-**	**-**	**1.81**
Dihedal angle	**Crystal**	**PyAm**	**Exp-Calc**	**1**	**Exp-Calc**	**PyAm**	**Exp-Calc**	**1**	**Exp-Calc**
N1-C20-C21-N2	-11.67	-48.690	37.020	-18.100	6.430	-48.930	37.260	-12.98	1.310

Table S13: Selected bond lengths (*Å*), angles (°) and dihedral angles (°) for the gas-phase optimized structures of **PmAm** ligand and **2** at the PBE1PBE-D3/TZVP and PBE1PBE/TZVP levels of theory as well as their deviations from the experimental parameters (Exp-Calc) along with mean absolute errors (MAE).

			PBE1PBE-D3				PBE1PBE		
Bond	**Crystal**	**PmAm**	**Exp-Calc**	**2**	**Exp-Calc**	**PmAm**	**Exp-Calc**	**2**	**Exp-Calc**
N1-C16	1.345	1.325	0.020	1.327	0.018	1.325	0.020	1.328	0.017
C16-C17	1.374	1.388	-0.014	1.387	-0.013	1.388	-0.014	1.387	-0.013
C17-C18	1.360	1.383	-0.023	1.384	-0.024	1.383	-0.023	1.384	-0.024
C18-N4	1.349	1.328	0.021	1.331	0.018	1.328	0.021	1.331	0.018
N4-C19	1.326	1.334	-0.008	1.326	0.000	1.334	-0.008	1.326	0.000
C19-N1	1.332	1.328	0.004	1.327	0.005	1.328	0.004	1.327	0.005
C19-C20	1.501	1.504	-0.003	1.495	0.006	1.505	-0.004	1.496	0.005
C20-N2	1.276	1.273	0.003	1.345	-0.069	1.273	0.003	1.276	0.000
C20-N3	1.352	1.367	-0.015	1.276	0.076	1.367	-0.015	1.346	0.006
Dy1-N1	2.614	-	-	2.641	-0.027	-	-	2.663	-0.049
Dy1-N2	2.454	-	-	2.512	-0.058	-	-	2.518	-0.064
Dy1-O1	2.322	-	-	2.357	-0.035	-	-	2.365	-0.043
Dy1-O2	2.351	-	-	2.341	0.010	-	-	2.349	0.002
Dy1-O3	2.356	-	-	2.304	0.052	-	-	2.308	0.048
Dy1-O4	2.312	-	-	2.343	-0.031	-	-	2.355	-0.043
Dy1-O5	2.327	-	-	2.364	-0.037	-	-	2.370	-0.043
Dy1-O6	2.330	-	-	2.355	-0.025	-	-	2.364	-0.034
MAE	**-**	**-**	**0.012**	**-**	**0.030**	**-**	**0.012**	**-**	**0.024**
Angles	**Crystal**	**PmAm**	**Exp-Calc**	**2**	**Exp-Calc**	**PmAm**	**Exp-Calc**	**2**	**Exp-Calc**
N1-Dy1-N2	55.59	-	-	61.63	-6.04	-	-	61.22	-5.63
O1-Dy1-O2	73.70	-	-	71.95	1.75	-	-	71.47	2.23
O3-Dy1-O4	73.66	-	-	73.75	-0.09	-	-	73.33	0.33
O5-Dy1-O6	72.84	-	-	71.68	1.16	-	-	71.22	1.62
O1-Dy1-N1	74.05	-	-	69.17	4.88	-	-	69.58	4.47
O2-Dy1-N2	74.58	-	-	76.68	-2.10	-	-	77.06	-2.48
O1-Dy1-O3	82.83	-	-	93.18	-10.35	-	-	94.88	-12.05
O1-Dy1-O5	75.85	-	-	75.20	0.65	-	-	75.00	0.85
O2-Dy1-O4	79.21	-	-	76.30	2.91	-	-	76.32	2.89
O2-Dy1-O6	144.42	-	-	146.34	-1.92	-	-	146.52	-2.10
MAE	**-**	**-**	**-**	**-**	**3.19**	**-**	**-**	**-**	**3.47**
Torsion angle	**Crystal**	**PmAm**	**Exp-Calc**	**2**	**Exp-Calc**	**PmAm**	**Exp-Calc**	**2**	**Exp-Calc**
N1-C19-C20-N2	0.39	-7.92	8.31	-0.29	0.68	-7.91	8.30	3.08	-2.69

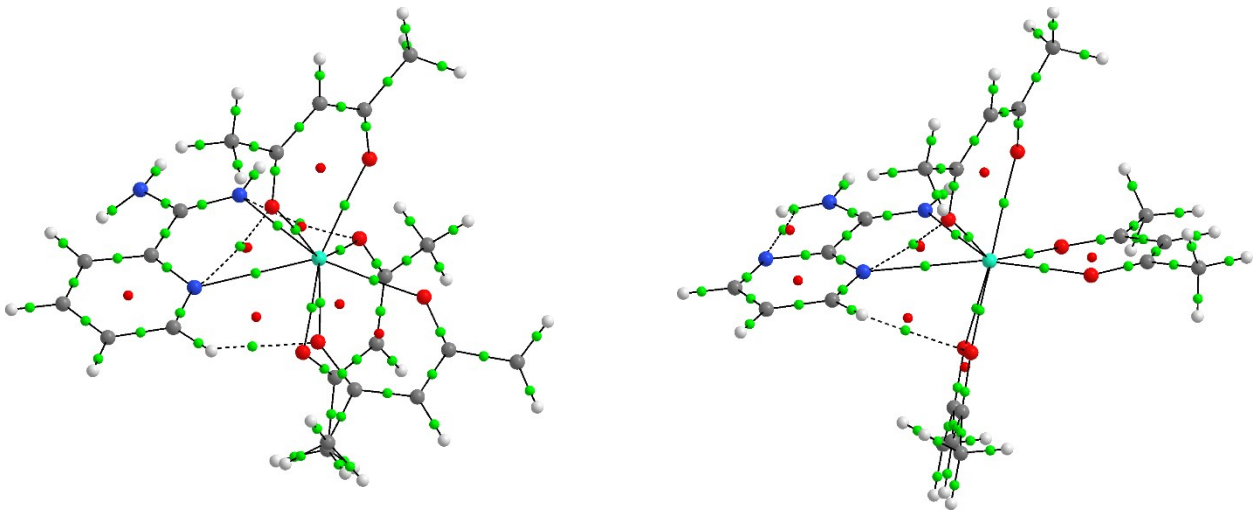

Figure S11. Bond baths (black lines), bond critical points (green spheres), and ring critical points (red spheres) for the PBE1PBE-D3/TZVP gas-phase optimized structures of **1** (left) and **2** (right).

Magnetic Measurements:

Direct current (dc) measurements

Magnetic susceptibility measurements for both samples were obtained using a Quantum Design SQUID magnetometer MPMS-XL7 operating between 1.8 and 300 K. Direct current (dc) measurements for **1** were performed on 15.5 mg of crushed polycrystalline sample, which was restrained with silicon grease and sealed in a polyethylene membrane for which diamagnetic corrections were applied. The sample was subjected to dc fields of 7 to -7 T while alternating current (ac) measurements took place under an applied external field of 1400 Oe. Similarly, direct current (dc) measurements for **2** were performed on 15.8 mg of crushed polycrystalline sample, which was restrained with silicon grease and sealed in a polyethylene membrane for which diamagnetic corrections were applied. The sample was subjected to dc fields of 7 to -7 T while alternating current (ac) measurements took place in the absence and presence of an applied external field of 1400 Oe. Magnetization (M) versus field (H) measurements were performed at 100K to asses any presence of paramagnetic impurity (Figure S12). The obtained data indicate absence of any paramagnetic impurities in the sample.

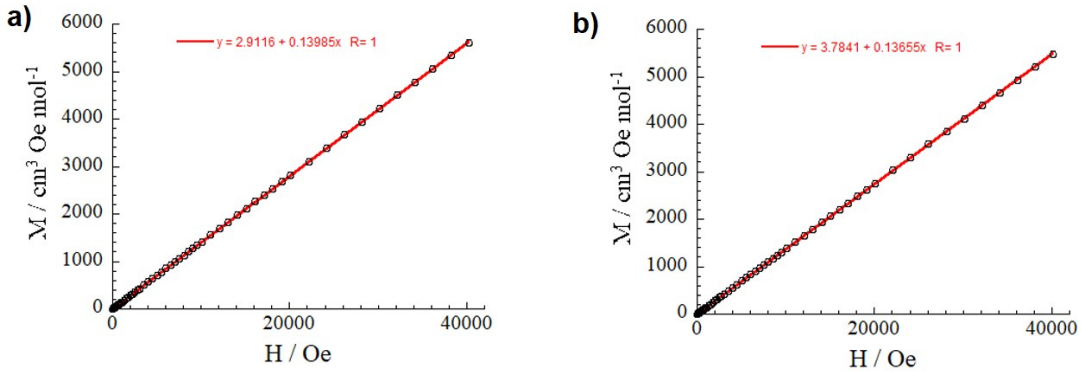

Figure S12. Magnetization (M) versus field (H)of **1** (a) and **2** (b) measured at 100K.

The dc magnetic susceptibility of both complexes was measured between 300 and 1.8 K under an applied field of 1000 Oe (Figure S13). Upon lowering of the temperature, both χT products exhibit a near identical gradual decrease from the room temperature value of 14.14 cm^3 K mol^{-1} for **1** and 14.15 cm^3 K mol^{-1} for **2**. The room temperature χT products for both complexes are in good agreement with the theoretical value for one Dy^{III} ion (S = 5/2, L = 5, $^6H_{15/2}$ g = 4/3, C = 14.17 cm^3 K mol^{-1}). The decrease of the χT product becomes more step below 5.5 K for **1** and 3.5 K for **2**, until it reaches a minimum of 9.07 cm^3 K mol^{-1} and 9.58 cm^3 K mol^{-1} at 1.8 K, respectively. This decrease in the low temperature region can be attributed to a combination of thermal depopulation of the Stark sublevels and/or the presence of significant magnetic anisotropy[53] and/or small but non-negligible antiferromagnetic intermolecular interactions between Dy^{III} centers (See Figure S13 and Table S15). To further confirm the magnetic anisotropy, magnetization measurements at low temperatures were performed. In both **1** and **2**, the magnetization plot (*M vs. H*) shows field dependence of the magnetization as it increases rapidly, upon increasing the field, reaching a value of 5.70 $N\mu_B$ for **1** and 5.40 $N\mu_B$ for **2**, at 1.9 K and 7 T (Figure S14). For both complexes the lack of saturation of the magnetization even at higher fields (7 T) suggests the presence of significant anisotropy and/or low-lying exited states. This is also supported by the lack of superimposition of the reduced magnetization curves (*M vs.* HT^{-1}).

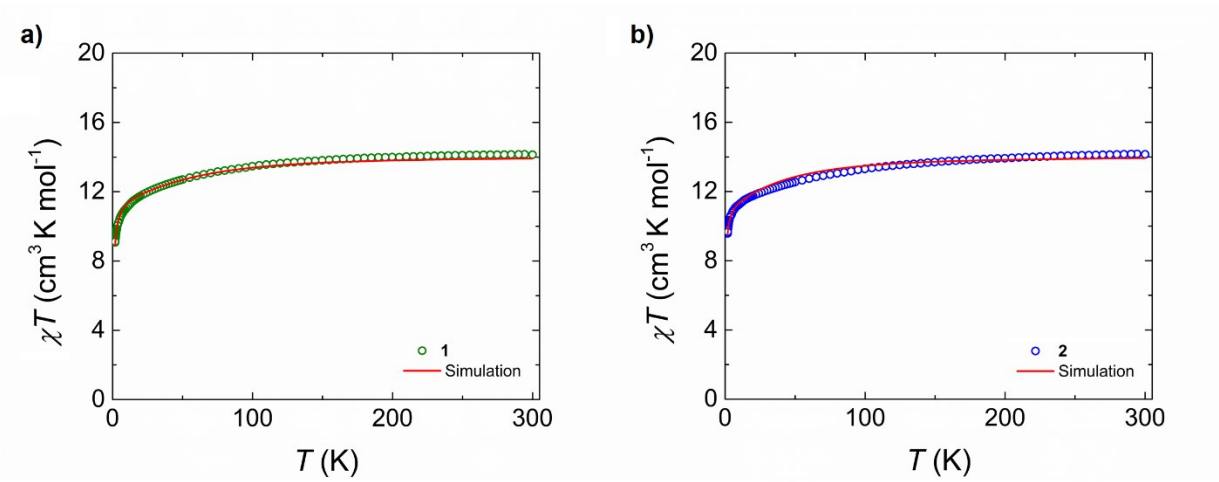

Figure S13. Variable temperature dc susceptibility of **1** (a, green circles) and **2** (b, blue circles) under an applied field of 1000 Oe. The solid red lines represent the calculated plots for **1** and **2** obtained from the SINGLE_ANISO calculations. To take into account average intermolecular interactions acting on the Dy(III) centers phenomenological zJ parameter with value of -0.070 and -0.044 for **1** and **2**, respectively, were included in the calculations. The negative values of the obtained zJ parameters indicates that the average intermolecular interactions are antiferromagnetic in nature, which is also reflected by the sign of the calculated dipolar coupling parameters (see Table S15).

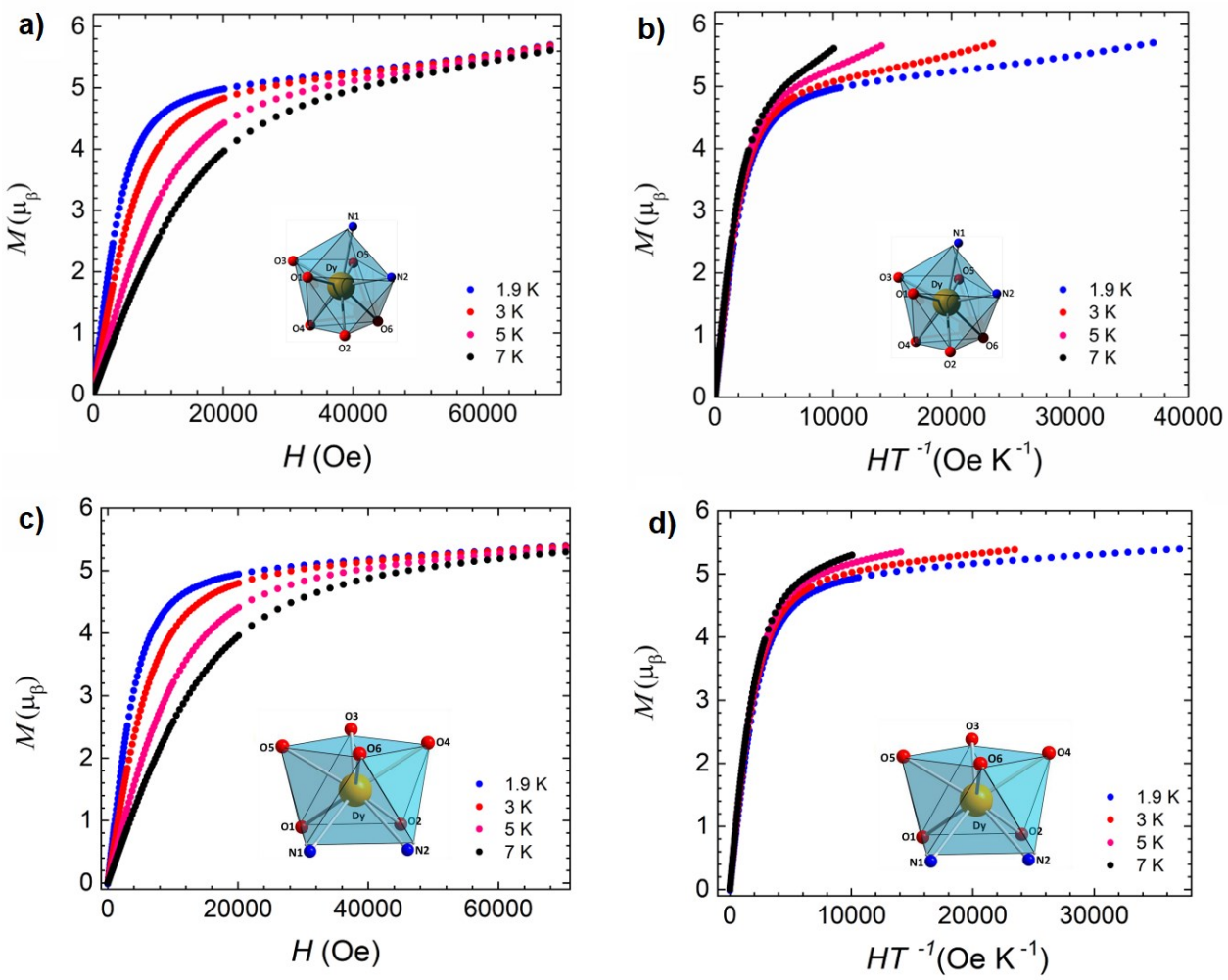

Figure S14. Magnetization and reduced magnetization curves of **1** (a and b, respectively) and **2** (c and d, respectively) at the indicated temperatures.

Alternating current (ac) measurements

The field and temperature dependent ac susceptibility of **1** and **2** was probed at varying fields and temperatures. The ac susceptibilities of these complexes were fitted using a generalized Debye model, to extract the relaxation times:

$$\chi' = \chi s + \frac{(\chi t - \chi s) * [1 + (2\pi vt)^{(1-\alpha)} sin\left(\frac{\alpha\pi}{2}\right)]}{[1 + \left(2(2\pi vt)^{(1-\alpha)}\right) sin\left(\frac{\alpha\pi}{2}\right) + (2\pi vt)^{2(1-\alpha)}]}$$

$$\chi'' = \frac{(\chi t - \chi s)(2\pi vt)^{(1-\alpha)} cos\left(\frac{\alpha\pi}{2}\right)}{[1 + \left(2(2\pi vt)^{(1-\alpha)}\right) sin\left(\frac{\alpha\pi}{2}\right) + (2\pi vt)^{2(1-\alpha)}]}$$

where the in-phase component χ' is the real and the out-of-phase χ'' the imaginary part of the susceptibility, χ_t is the isothermal susceptibility, χ_s the adiabatic susceptibility, v is the linear frequency, the α parameter shows the distribution of the relaxation times and t is the relaxation time of the magnetization.

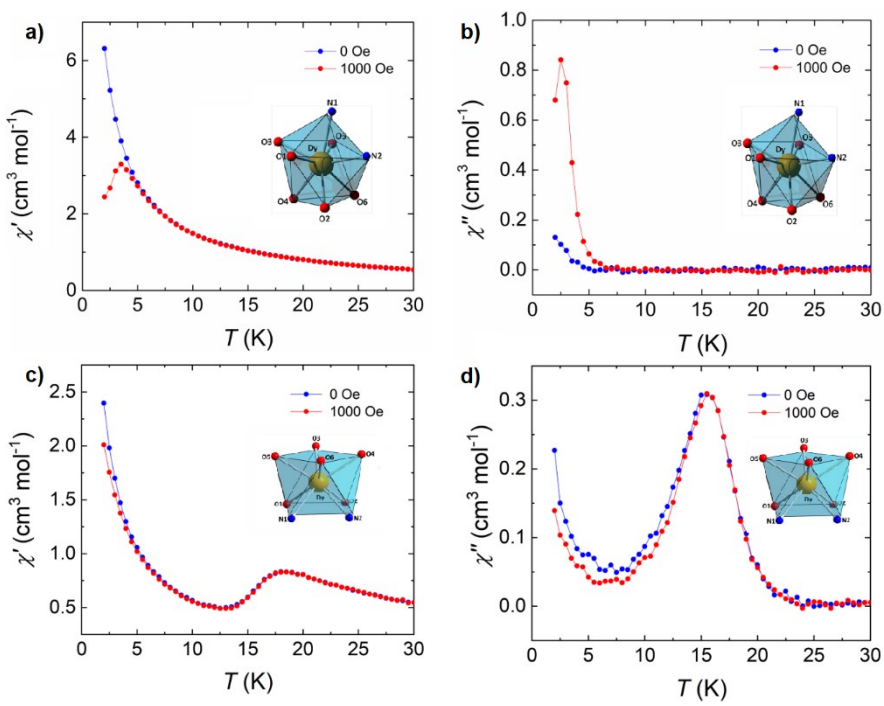

Figure S15. AC susceptibility measurement performed at variable temperatures under zero (blue) and applied dc field of 1000 Oe (red) for **1** (a, b) and **2** (c, d) at 1488 Hz.

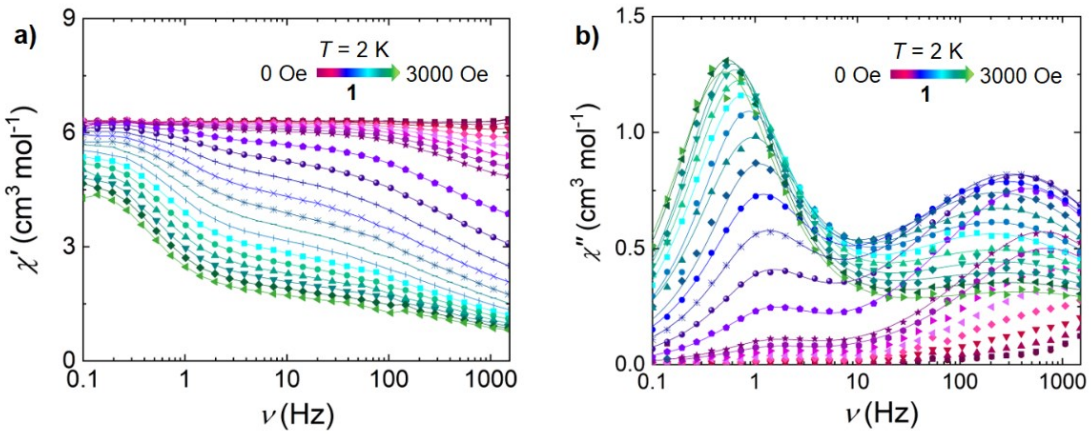

Figure S16. The in-phase (χ')(a) and out-of-phase (χ'')(b) magnetic susceptibility of **1** at 2 K at the indicated field region. For the χ' the solid lines serve as a guide to the eye, while for the χ'' the solid lines represent the best-fit to the generalized Debye model (*vide supra*).

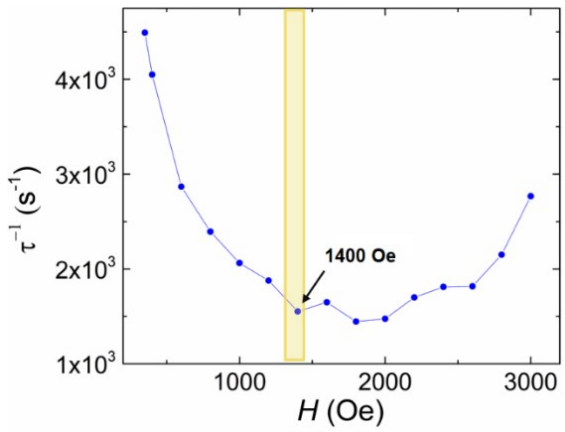

Figure S17. Field dependence of the relaxation times (τ) of the high-frequency process for **1** at 2 K. The minimum represents the optimal field for which the relaxation time is longest and quantum tunneling of the magnetization is reduced (1400 Oe; yellow highlight). This is the field at which temperature dependent relaxation studies were completed at (*vide infra*).

Table S14: Best-fit parameters to the generalized Debye model for the frequency dependence of the out-of-phase magnetic susceptibility (χ'') as a function of field for **1**. Data collected at 2 K.

	High-frequency process					*Low-frequency process*				
H (Oe)	τ_1	α_1	χ_{s1}	χ_{t1}	χ_{t1}- χ_{s1}	τ_2	α_2	χ_{s2}	χ_{t2}	χ_{t2}- χ_{s2}
350	2.226E-4	0.326	2.888	4.602	1.714	0.12	0	3.728	3.842	0.114
400	2.469E-4	0.331	2.765	4.735	1.970	0.119	0	3.665	3.825	0.16
600	3.486E-4	0.376	1.653	4.49	2.837	0.122	0	3.565	3.935	0.37
800	4.177E-4	0.438	1.585	5.032	3.447	0.128	0.013	3.441	4.059	0.618
1000	4.847E-4	0.477	1.875	5.625	3.75	0.138	0.018	2.99	3.893	0.903
1200	5.324E-4	0.506	1.832	5.668	3.836	0.15	0.018	3.141	4.33	1.189
1400	6.440E-4	0.518	1.899	5.601	3.702	0.16	0	3.075	4.474	1.399
1600	6.061E-4	0.518	1.827	5.173	3.346	0.182	0.054	2.583	4.417	1.834
1800	6.916E-4	0.54	2.15	5.35	3.2	0.194	0.007	2.703	4.619	1.916
2000	6.776E-4	0.527	2.33	5.17	2.84	0.218	0.037	3.277	5.499	2.222
2200	5.879E-4	0.579	3.385	6.225	2.84	0.239	0.027	2.853	5.147	2.294
2400	5.52E-4	0.581	3.527	6.083	2.556	0.256	0.023	2.791	5.203	2.412
2600	5.501E-4	0.604	3.587	6.016	2.429	0.272	0.006	2.589	4.99	2.401
2800	4.465E-4	0.607	3.706	5.896	2.19	0.302	0.031	2.495	5.065	2.57
3000	3.613E-4	0.62	3.799	5.803	2.004	0.319	0.054	2.488	5.072	2.584

Table S15: Calculated intermolecular dipolar coupling constants (*J*) between the neighboring Dy(III) ions in **1** and **2**. *r* is the distance between the neighboring Dy(III) ions. Calculations were carried out at the SA-CASSCF/SO-RASSI level of theory.

DyPyAm		DyPmAm	
r (Å)	*J* (cm^{-1})	*r* (Å)	*J* (cm^{-1})
6.516	-0.553	6.660	-0.500
8.303	-0.174	6.660	-0.500
8.303	-0.174	8.711	0.168
9.019	-0.184	9.827	-0.039
9.167	-0.039	9.827	-0.039
9.167	-0.039	10.077	0.095
10.623	0.204	10.077	0.095
10.623	0.204	10.871	0.014
11.348	-0.027	10.871	-0.014
11.420	-0.137	11.829	-0.017
11.420	0.137	12.324	0.028
11.893	-0.066	12.684	0.114
11.954	0.091	12.793	-0.053
11.954	0.091	12.793	0.053
12.949	-0.065	12.799	0.135
14.041	0.027	12.799	0.135
14.041	0.027	13.565	-0.060
14.897	-0.038	13.835	0.102
15.037	0.056	14.694	0.002
15.092	-0.001	14.998	0.031
16.279	0.068	15.245	-0.041
16.380	0.001	15.245	-0.041
17.631	-0.005	15.750	-0.039
17.631	-0.005	15.983	0.045
18.031	-0.003	17.478	-0.026
18.304	-0.005	19.223	-0.020

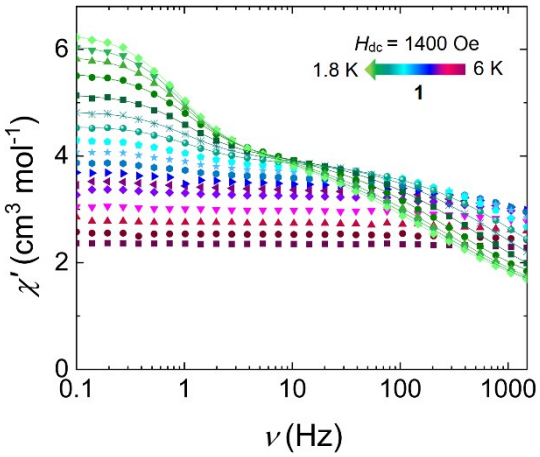

Figure S18. The in-phase (χ') magnetic susceptibility of **1** at 1400 Oe at the indicated temperature region. The solid lines represent the best-fit to the generalized Debye model (*vide supra*).

Table S16: Best-fit parameters to the generalized Debye model for the frequency dependence of the in-phase magnetic susceptibility (χ') as a function of temperature for **1**. Data collected under an applied static field of 1400 Oe.

	High frequency process					*Low frequency process*				
T (K)	τ_1	α_1	χ_{s1}	χ_{t1}	χ_{t1}- χ_{s1}	τ_2	α_2	χ_{s2}	χ_{t2}	χ_{t2}- χ_{s2}
2.8	1.005E-4	0.424	0	3.084	3.084	0.151	0.072	0.865	1.479	0.614
2.6	1.84E-4	0.414	0.258	3.29	3.032	0.153	0.083	0.729	1.557	0.828
2.4	2.964E-4	0.437	0.171	3.358	3.187	0.156	0.059	0.766	1.808	1.042
2.2	5.767E-4	0.401	0	2.871	2.871	0.152	0.104	1.228	2.713	1.485
2	6.177E-4	0.502	0	3.512	3.512	0.17	0.053	0.808	2.402	1.594
1.9	7.257E-4	0.515	0.158	3.732	3.574	0.177	0.051	0.635	2.412	1.777
1.8	9.091E-4	0.506	0.184	3.636	3.452	0.185	0.066	0.722	2.721	1.999

Table S17: Best-fit parameters to the generalized Debye model for the frequency dependence of the out-of-phase magnetic susceptibility (χ'') as a function of temperature for **1**. Data collected under an applied static field of 1400 Oe.

	High frequency process					*Low frequency process*				
T (K)	τ_1	α_1	χ_{s1}	χ_{t1}	χ_{t1}- χ_{s1}	τ_2	α_2	χ_{s2}	χ_{t2}	χ_{t2}- χ_{s2}
2.8	8.895E-5	0.423	4.641	7.871	3.23	0.146	0.079	3.473	4.087	0.614
2.6	1.556E-4	0.435	3.728	7.061	3.333	0.148	0.044	3.399	4.161	0.762
2.4	2.674E-4	0.446	3.126	6.476	3.35	0.149	0.044	3.282	4.278	0.996
2.2	4.22E-4	0.486	3.04	6.562	3.522	0.156	0.032	3.148	4.412	1.264
2	5.989E-4	0.515	2.990	6.612	3.622	0.164	0.03	3.02	4.54	1.52
1.9	7.742E-4	0.519	2.991	6.611	3.62	0.173	0.029	2.932	4.628	1.696
1.8	8.848E-4	0.533	2.971	6.631	3.66	0.179	0.034	2.854	4.706	1.852

Fitting of the relaxation times: The relaxation times of the magnetization of the ac susceptibility of **1** and **2** were fitted to unravel the relaxation mechanisms of the magnetization. The primary four mechanisms through which the relaxation of the magnetization can occur are QTM, Raman, Orbach and/or direct processes and can be expressed by the following equation[54]:

$$\tau(T,H)^{-1} = \tau_{QTM(T,H)}^{-1} + \tau_{Raman(T)}^{-1} + \tau_{Orbach(T)}^{-1} + \tau_{Direct(T,H)}^{-1}$$

$$\tau(T,H)^{-1} = \frac{B_1^{-1}}{1 + B_2 H^2} + CT^n + \tau_0 \exp\left(\frac{-U_{eff}}{kT}\right) + AH^4T$$

For the temperature dependent relaxation times, the QTM component can be expressed as a single variant and it is symbolized as: τ_{QTM}^{-1}.

For the relaxation times of the high-frequency process of the ac susceptibility of **1**, measured under an applied field of 1400 Oe between 2.8 and 1.8 K, a satisfactory fit was obtained for a combination of QTM and Raman, as described by eqn (1). The low-frequency process in the same temperature region can only be attributed to QTM and was fitted accordingly by eqn (2) (Figure S19). Equations 1 and 2 are given bellow.

$$\tau^{-1} = \tau_{QTM}^{-1} + CT^n \qquad (1)$$

$$\tau^{-1} = \tau_{QTM}^{-1} \qquad (2)$$

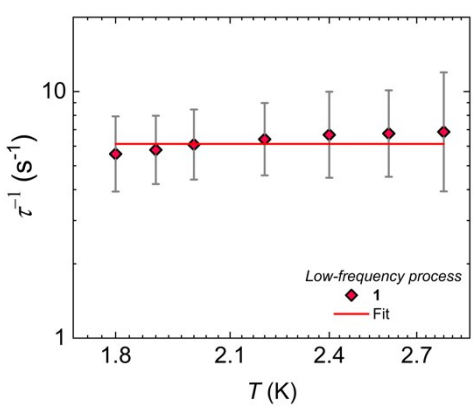

Figure S19. Temperature dependence of the relaxation times (τ) for the low-frequency process for compound **1**. The solid red lines represent the best fit (see Table S18 for best fit parameters) to **eqn. 2**. The estimated standard deviations of the relaxation times have been calculated from the α-parameters of the generalized Debye fit with the log-normal distribution.[52]

Table S18: Best-fit parameters for the magnetic relaxation for compound **1** and **2** obtained from the fit of the frequency dependent relaxation times.

Parameters		1 H_{dc} = 1400 Oe		2 H_{dc} = 0 Oe		2 H_{dc} = 1400 Oe
		High Frequency process	*Low frequency process*	*Main process*	*Minor process*	
QTM	τ_{QTM} (s)	(1.12 ± 0.09) x 10^{-3}	(1.63 ± 0.05) x 10^{-1}	(4.14 ± 1.7) × 10^{-2}	(5.89 ± 0.82) × 10^{-3}	
Raman	C (s^{-1} K^{-n})	2.30 ± 0.71		(3.22 ± 0.13) × 10^{-4}	(1.64 ± 0.66) × 10^{-4}	(1.78 ± 0.12) × 10^{-4}
	n	8.16 ± 0.30		6.2 ± 0.04	6.58 ± 0.05	6.37 ± 0.03

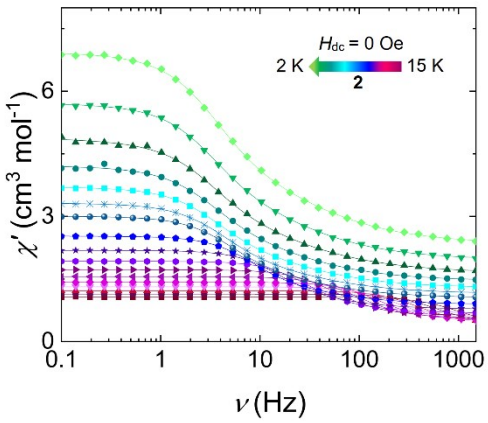

Figure S20. Frequency dependence of the in-phase (χ') magnetic susceptibility in the indicated temperature range for compound **2** in the absence of an applied field. Solid lines represent fits to the generalized Debye model (*vide supra*).

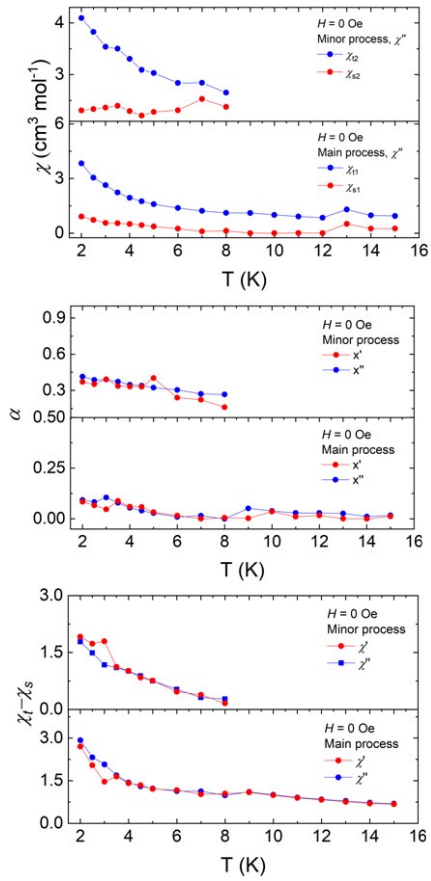

Figure S21. Data obtained from the generalised Debye fits of χ' and χ'' frequency dependent ac data collected in the absence of an applied static field (H_{dc} = 0 Oe) for compound **2**. Temperature dependence of χ_t and χ_s (top), α (middle) and χ_t- χ_s (bottom).

Table S19: Best-fit parameters to the generalized Debye model for the frequency dependence of the in-phase magnetic susceptibility (χ') as a function of temperature for **2**. Data collected in the absence of an applied field (H_{dc} = 0 Oe).

T (K)	τ_1	α_1	χ_{s1}	χ_{t1}	χ_{t1}- χ_{s1}	τ_2	α_2	χ_{s2}	χ_{t2}	χ_{t2}- χ_{s2}
15	1.593E-4	0.012	0.39	1.064	0.674					
14	2.635E-4	0	0.434	1.136	0.702					
13	4.077E-4	9.555E-4	0.458	1.216	0.758					
12	6.307E-4	0.017	0.483	1.312	0.829					
11	9.942E-4	0.01	0.526	1.421	0.895					
10	0.162E-2	0.036	0.568	1.557	0.989					
9	0.275E-2	0.003	0.633	1.723	1.09					
8	0.551E-2	0.005	0.68	1.726	1.046	0.103E-2	0.161	0	0.161	0.161
7	0.01	4.727E-4	0.729	1.755	1.026	0.248E-2	0.222	0.045	0.429	0.384
6	0.019	0.016	0.663	1.832	1.169	0.284E-2	0.24	0.227	0.694	0.467
5	0.031	0.033	0.642	1.85	1.208	0.542E-2	0.403	0.403	1.161	0.758
4.5	0.037	0.058	0.551	1.893	1.342	0.574E-2	0.33	0.595	1.433	0.838
4	0.043	0.06	0.517	1.931	1.414	0.675E-2	0.332	0.767	1.783	1.016
3.5	0.046	0.088	0.398	2.041	1.643	0.701E-2	0.336	1.055	2.178	1.123
3	0.048	0.047	0.594	2.06	1.466	0.011	0.392	1.044	2.84	1.796
2.5	0.047	0.067	0.544	2.585	2.041	0.008	0.352	1.41	3.141	1.731
2	0.044	0.084	1.169	3.872	2.703	0.006	0.37	1.167	3.08	1.913

Table S20: Best-fit parameters to the generalized Debye model for the frequency dependence of the out-of-phase magnetic susceptibility (χ'') as a function of temperature for **2**. Data collected in the absence of an applied field (H_{dc} = 0 Oe).

T (K)	τ_1	α_1	χ_{s1}	χ_{t1}	χ_{t1}- χ_{s1}	τ_2	α_2	χ_{s2}	χ_{t2}	χ_{t2}- χ_{s2}
15	1.569E-4	0.017	0.254	0.946	0.692					
14	2.471E-4	0.012	0.252	0.979	0.727					
13	3.885E-4	0.026	0.511	1.298	0.787					
12	6.177E-4	0.029	0.002	0.846	0.844					
11	9.773E-4	0.029	0.006	0.916	0.91					
10	0.161E-2	0.039	0.002	1.005	1.003					
9	0.273E-2	0.052	0.005	1.108	1.103					
8	0.553E-2	0	0.127	1.114	0.987	0.128E-2	0.266	2.377	2.653	0.276
7	0.992E-2	0.015	0.099	1.224	1.125	0.155E-2	0.271	2.528	2.842	0.314
6	0.019	0.009	0.247	1.382	1.135	0.302E-2	0.304	2.311	2.839	0.528
5	0.031	0.028	0.366	1.591	1.225	0.472E-2	0.323	2.279	3.031	0.752
4.5	0.037	0.04	0.445	1.746	1.301	0.548E-2	0.34	2.207	3.093	0.886
4	0.046	0.054	0.505	1.94	1.435	0.591E-2	0.347	2.295	3.305	1.01
3.5	0.043	0.079	0.545	2.233	1.688	0.558E-2	0.372	2.399	3.501	1.102
3	0.043	0.105	0.566	2.636	2.07	0.48E-2	0.39	2.363	3.537	1.174
2.5	0.043	0.083	0.727	3.048	2.321	0.489E-2	0.387	2.334	3.826	1.492
2	0.041	0.093	0.913	3.833	2.92	0.376E-2	0.415	2.307	4.093	1.786

Similarly to **1**, the relaxation times for both processes of the ac susceptibility of **2**, measured in the absence of an external dc magnetic field between 15 and 2 K, were satisfactory fitted to a combination of QTM and Raman, as described by eqn (1) (Figure S22, *vide infra*). However, with the introduction of an external dc field of 1400 Oe, the minor process and the QTM contribution are suppressed, as expected, and the main relaxation process of the magnetization can only be described as a Raman process. Equations 1 and 3 are given bellow.

$$\tau^{-1} = \tau_{QTM}^{-1} + CT^n \qquad (1)$$

$$\tau^{-1} = CT^n \qquad (3)$$

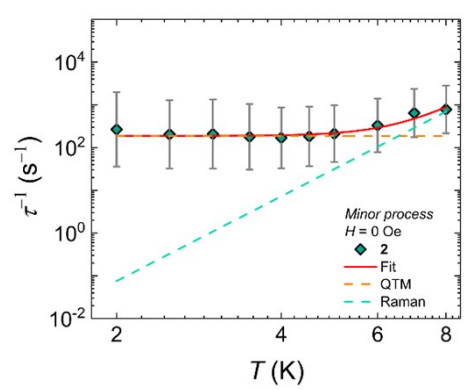

Figure S22. Temperature dependence of the relaxation times (τ) for the minor process for compound **2**. The solid red lines represent the best fit to **eqn. 1** (see Table S18 for best fit parameters). The orange and teal dashed lines are the individual components of the magnetization relaxation for QTM and Raman processes, respectively. The estimated standard deviations of

the relaxation times have been calculated from the α-parameters of the generalized Debye fit with the log-normal distribution.[52]

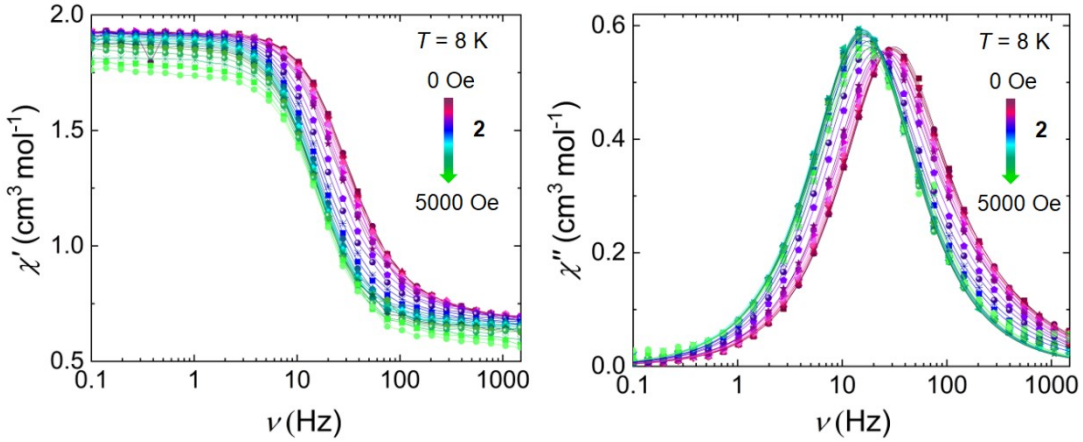

Figure S23. The in-phase (χ')(left) and out-of-phase (χ'')(right) magnetic susceptibility at 8 K at the indicated field region. For the χ' the solid lines serve as a guide to the eye, while for the χ'' the solid lines represent the best-fit to the generalized Debye model (*vide supra*).

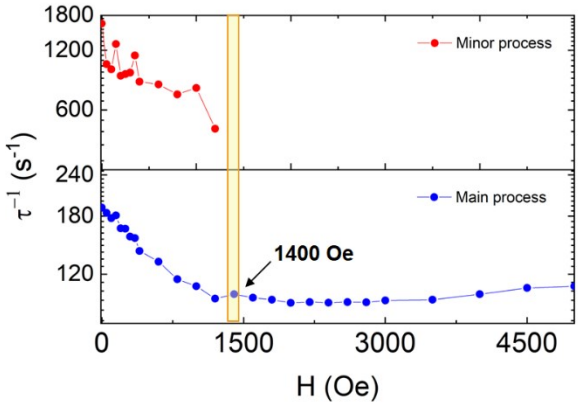

Figure S24. Field dependence of the relaxation times (τ) of both processes for **2** at 8 K, indicating the field that was selected where the second process is suppressed (highlighted in yellow).

Table S21: Best-fit parameters to the generalized Debye model for the frequency dependence of the out-of-phase magnetic susceptibility (χ'') as a function of field for **2**. Data collected at 8 K.

H (Oe)	τ_1	α_1	χ_{s1}	χ_{t1}	χ_{t1}- χ_{s1}	τ_2	α_2	χ_{s2}	χ_{t2}	χ_{t2}- χ_{s2}
0	0.523E-2	0.015	0.072	1.169	1.098	6.109E-4	0.254	2.43	2.6	0.17
50	0.543E-2	0.004	0.104	1.137	1.033	9.796E-4	0.266	2.4	2.63	0.23
100	0.564E-2	0	0.113	1.128	1.016	0.104E-2	0.225	2.4	2.633	0.233
150	0.553E-2	0.015	0.079	1.162	1.082	7.76E-4	0.235	2.428	2.602	0.174
200	0.605E-2	0	0.119	1.122	1.004	0.112E-2	0.228	2.389	2.641	0.252
250	0.607E-2	0.011	0.101	1.14	1.039	0.1E-2	0.235	2.409	2.621	0.212
300	0.641E-2	0.013	0.098	1.143	1.044	0.11E-2	0.236	2.407	2.623	0.216
350	0.648E-2	0.019	0.078	1.163	1.085	8.858E-4	0.235	2.429	2.601	0.172
400	0.709E-2	0	0.109	1.133	1.024	0.12E-2	0.151	2.404	2.626	0.222
600	0.764E-2	0.022	0.118	1.201	1.083	0.124E-2	0.251	2.426	2.604	0.178
800	0.864E-2	0.007	0.118	1.181	1.063	0.139E-2	0.259	2.42	2.61	0.19
1000	0.907E-2	0.013	0.116	1.234	1.118	0.129E-2	0.30002	2.445	2.585	0.14
1200	0.989E-2	1.136E-5	0.148	1.241	1.093	0.207E-2	0.24495	2.435	2.595	0.16
1400	0.959E-2	0.034	0.184	1.416	1.232					
1600	0.983E-2	0.032	0.192	1.428	1.235					
1800	0.997E-2	0.026	0.012	1.248	1.236					
2000	1.018E-2	0.036	0.008	1.259	1.244					
2200	1.014E-2	0.025	0.013	1.247	1.234					
2400	1.017E-2	0.025	0.015	1.245	1.229					
2600	1.014E-2	0.027	0.017	1.244	1.227					
2800	1.015E-2	0.027	0.019	1.241	1.221					
3000	1.002E-2	0.032	0.017	1.243	1.226					
3500	0.997E-2	0.034	0.025	1.235	1.21					
4000	0.96E-2	0.049	0.028	1.248	1.22					
4500	0.92E-2	0.061	0.016	1.244	1.227					
5000	0.91E-2	0.06	0.034	1.226	1.192					

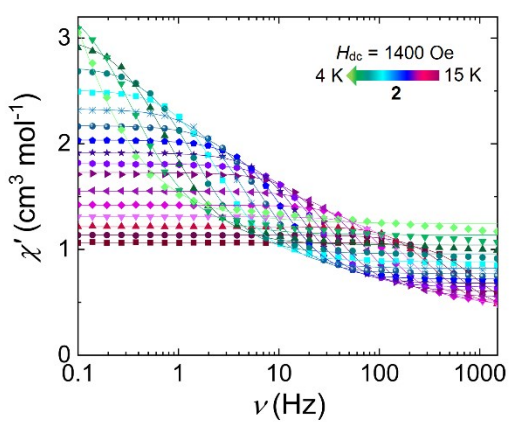

Figure S25. Frequency dependence of the in-phase (χ') magnetic susceptibility in the indicated temperature range for compound **2** under an applied static field of 1400 Oe. Solid lines represent fits to the generalized Debye model (*vide supra*).

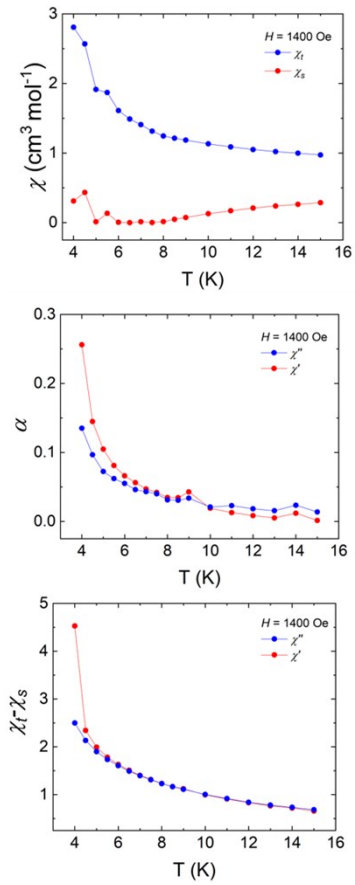

Figure S26. Data obtained from the generalised Debye fits of χ' and χ'' frequency dependent ac data collected under an applied static field of 1400 Oe for compound **2**. Temperature dependence of χ_t and χ_s (top), α (middle) and χ_t- χ_s (bottom).

Table S22: Best-fit parameters to the generalized Debye model for the frequency dependence of the in-phase magnetic susceptibility (χ') as a function of field for **2**. Data collected under an applied field of 1400 Oe.

T (K)	τ	α	χ_s	χ_t	χ_t- χ_s
15	1.791E-4	0.001	0.406	1.065	0.659
14	2.894E-4	0.012	0.415	1.136	0.721
13	4.776E-4	0.005	0.45	1.217	0.767
12	7.877E-4	0.009	0.477	1.31	0.833
11	0.133E-2	0.013	0.511	1.42	0.909
10	0.237E-2	0.019	0.556	1.553	0.997
9	0.464E-2	0.043	0.606	1.729	1.123
8.5	0.657E-2	0.035	0.644	1.812	1.168
8	0.956E-2	0.035	0.68	1.914	1.234
7.5	1.44E-2	0.042	0.72	2.036	1.316
7	2.244E-2	0.047	0.769	2.173	1.404
6.5	3.608E-2	0.056	0.821	2.331	1.51
6	6.056E-2	0.066	0.883	2.515	1.632
5.5	0.107	0.081	0.957	2.74	1.783
5	0.206	0.105	1.041	3.035	1.994

4.5	0.445	0.145	1.137	3.48	2.343
4	2.265	0.256	1.243	5.772	4.529

Table S23: Best-fit parameters to the generalized Debye model for the frequency dependence of the out-of-phase magnetic susceptibility (χ'') as a function of field for **2**. Data collected under an applied field of 1400 Oe.

T (K)	τ	α	χ_s	χ_t	χ_t- χ_s
15	1.708E-4	0.014	0.287	0.973	0.686
14	2.835E-4	0.024	0.262	0.998	0.736
13	4.673E-4	0.016	0.239	1.021	0.782
12	7.782E-4	0.018	0.21	1.05	0.84
11	0.133E-2	0.023	0.171	1.089	0.918
10	0.239E-2	0.021	0.128	1.132	1.004
9	0.459E-2	0.034	0.074	1.186	1.112
8.5	0.66E-2	0.031	0.047	1.213	1.166
8	0.959E-2	0.031	0.014	1.246	1.232
7.5	1.448E-2	0.04	0.002	1.314	1.312
7	2.25E-2	0.043	0.012	1.408	1.396
6.5	3.635E-2	0.046	1.086E-4	1.49	1.49
6	6.072E-2	0.055	0.006	1.611	1.605
5.5	0.107	0.062	0.133	1.87	1.737
5	0.202	0.072	0.013	1.914	1.901
4.5	0.402	0.097	0.434	2.568	2.134
4	0.962	0.135	0.311	2.809	2.498

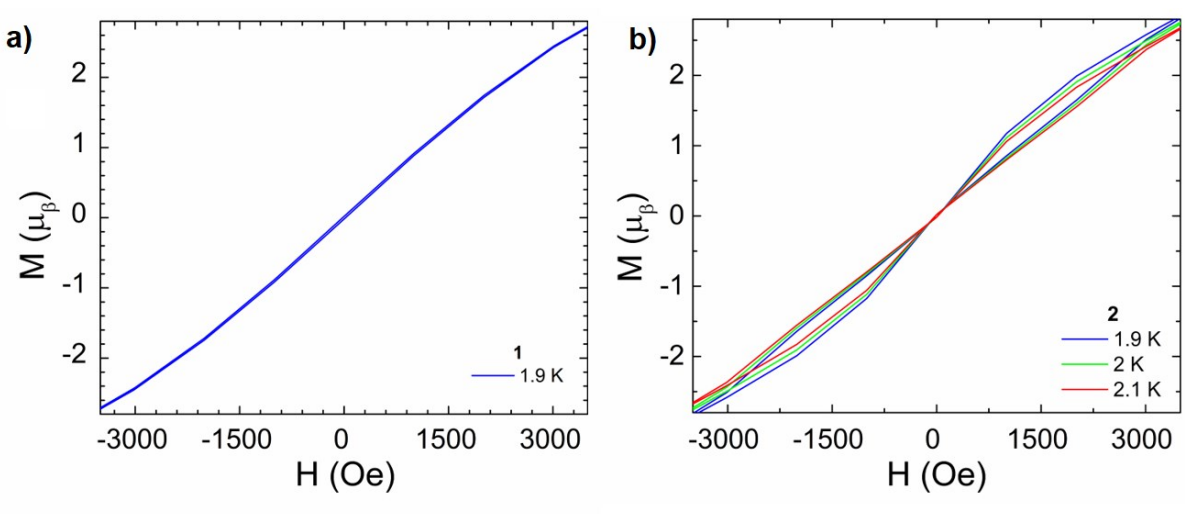

Figure S27. a) Magnetic hysteresis data for **1** at 1.9 K. b) Magnetic hysteresis data for **2** in the temperature range of 1.9 to 2.1 K. For both measurements were performed with an average sweep rate of 25 Oe/s.

Theoretical Studies

Density functional theory (DFT) calculations were carried out for **PyAm**, **PmAm**, **1**, $\mathbf{1_Y}$, **2**, $\mathbf{2_Y}$, [Y(acac)$_3$], [Y(PyAm)(acac)$_2$]$^+$, [Y(PmAm)(acac)$_2$]$^+$, [Dy(acac)$_3$], [Dy(PyAm)(acac)$_2$]$^+$, [Dy(PmAm)(acac)$_2$]$^+$ and [acac]$^-$ using the PBE1PBE[14, 15] exchange-correlation functional in combination with Aldrich's *et*. *al*. polarized triple-ζ valence quality basis set (TZVP)[16, 17] for all atoms, except for Dy, for which Cundari's and Stevens' polarized double-ζ valence quality basis set was used.[18] The core electrons of Y and Dy atoms were described using the (relativistic) effective core potentials develop by Preuss *et. al.*[19] and Cundari & Stevens,[18] respectively. All DFT calculations were performed with and without Grimme's empirical dispersion correction (D3)[20] in conjunction with Becke-Johson (BJ) damping factor.[21] The geometries of the investigated systems were fully optimized without geometry constraints in the gas-phase. The frequency analyses were carried out for all optimized structures to ensure that they correspond to true minima (no negative frequencies) on the potential energy hypersurface (PES). In addition to the geometry optimizations, the relaxed PES scans were carried out for the **PyAm** and **PmAm** ligands along the dihedral angle N1-C20-C21-N2 and N1-C19-C20-N2, respectively, at the PBE1PBE-D3 level of theory. To get more computational insight of the investigated systems, atoms in molecules (AIM)[22] analyses were performed for the **PyAm**, **PmAm**, **1**, and **2** using the electron density obtained from the PBE1PBE-D3 and PBE1PBE calculations. Also, the electron localization functions (ELF)[23] were calculated for **PyAm** and **PmAm** ligands using the calculated PBE1PBE-D3 electron density. All gas-phase DFT calculations were performed with Gaussian16[24] quantum chemistry program, whereas atoms in molecules (AIM) analyses and electron localization functions (ELF) were carried out with the AIMALL[25] and TopMod[23, 26] program packages, respectively.

To obtain the lattice stabilization energies for **2**, the crystal structure of its hypothetical Y analog, $\mathbf{2_Y}$, was optimized without constraints in the solid-state using the periodic-boundary DFT calculations. The same exchange-correlation functional (PBE1PBE) and dispersion correction (D3) were used in the solid-state calculations as in the gas-phase calculations, but Bredow's *et. al.*[27, 28] polarized triple-ζ valence quality basis set (pob-TZVP) specially designed for the solid-state calculations was employed, in the periodic-boundary DFT calculations instead of Aldrich's polarized triple-ζ valence basis set.[16, 17] The solid-state calculations were carried out with the Crystal17 program package.[29, 30] No solid-state calculations were carried out for **1** as the Crystal17 do not support $P2_1/n$ space group.

The electronic structures of **1** and **2** were modelled using the state averaged complete active space self-consistent field (SA-CASSCF) method[31–33] in conjunction with the restricted active space state interaction (RASSI)[34–36] method to treat the spin-orbit interaction. The SA-CASSCF/RASSI calculations were performed for the crystal structures of **1** and **2** in which only the positions of hydrogen atoms were optimized at the PBE1PBE-D3/TZVP level of theory prior to the SA-CASSCF/RASSI calculations. The relativistically contracted natural atomic orbital (ANO-RCC) basis set developed by Roos. *et. al.* was used for all atoms in the SA-CASSCF/RASSI calculations; a polarized triple-ζ valence quality (ANO-RCC-TZVP) for Dy and a polarized double-ζ valence quality (ANO-RCC-DZVP) for all other atoms.[37, 38] Scalar

relativistic effects were treated employing the exact two-component (X2C) transformation.[39–41] Cholesky decomposition with a threshold value of 10^{-8} was applied to speed up calculations by reducing the size of the two-electron integrals. In the SA-CASSCF calculations, all sextet (21), quartet (228) and doublet (490) roots arising from nine electrons in seven 4f-orbitals were solved. We also calculated the extended multistate complete active space perturbation theory at the second order (XMS-CASPT2)[42, 43] corrections for the eigenvalues of the lowest 21 doublets to investigate the influence of the dynamic electron correlation on the splitting of energy levels in the ground multiplet $^6H_{15/2}$ of **1** and **2**. No mixing of the SA-CASSCF eigenstates was taken into account in XMS-CASPT2 calculations. Out of the calculated SA-CASSCF (XMS-CASPT2) roots, the lowest 21 (21) sextet, 128 quartet (-), and 130 (-) doublet roots were mixed by spin-orbit coupling in the subsequent SO-RASSI calculations. The obtained SO-RASSI wave functions were used to extract the ***g***-tensors, crystal field parameters and qualitative relaxation barrier for **1** and **2**. Moreover, the dipolar coupling between neighboring Dy(III) ions were calculated using the point-dipolar approximation as implemented in POLY_ANISO program[44,45]. The dipolar coupling parameter was then extracted from the eigenvalues of the dipolar interaction using the following Hamiltonian:

$$\hat{H} = -J\hat{S}_1\hat{S}_2 \quad (1),$$

where J is the dipolar coupling parameter and $\hat{S}1$ and $\hat{S}2$ are the projections of pseudospins (S = 1/2) describing the ground KDs on the Dy center of 1 and 2, respectively. Dipolar couplings were calculated because it has been shown that small but non-negligible dipolar interactions between neighboring ions can facilitate the QTM.[46, 47] OpenMolcas[48] quantum chemistry code in combination of SINGLE_ANISO[49–51] and POLY_ANISO[44, 45] modules were employed in the electronic structures and magnetic calculations.

We acknowledge Prof. Heikki Tuononen and grants of computer capacity from the Finnish Grid and Cloud Infrastructure (persistent identifier urn:nbn:fi:research-infras-2016072533) for providing computational resources for the project.

Table S24: Calculated energies and **g**-tensors for each KDs arising from the crystal-field split of ground $^6H_{15/2}$ multiplet of **1** as well as angle (ϑ) between the principal magnetic axes of the ground and excited Kramers doublets at the SA-CASSCF/RASSI level of theory. Energy values given in parentheses are calculated at the SA-CASSCF/XMS-CASPT2/RASSI level of theory.

KD	*Energy* (cm^{-1})		g_x	g_y	g_z	ϑ (°)
1	0.000	(0.000)	0.024	0.043	19.308	-
2	118.792	(120.267)	2.006	6.549	11.752	59.921
3	139.497	(141.548)	8.297	5.590	0.711	121.750
4	181.209	(184.178)	3.014	5.509	10.183	86.000
5	221.089	(223.933)	1.431	1.732	14.785	90.454
6	289.382	(294.154)	0.069	0.126	18.732	127.445
7	345.546	(351.797)	0.024	0.081	16.527	79.306
8	429.464	(437.139)	0.035	0.080	18.650	55.899

Table S25: Calculated energies and **g**-tensors for each KDs arising from the crystal-field split of ground $^6H_{15/2}$ multiplet of **2** as well as angle (ϑ) between the principal magnetic axes of the ground and excited Kramers doublets at the SA-CASSCF/RASSI level of theory. Energy values given in parentheses are calculated at the SA-CASSCF/XMS-CASPT2/RASSI level of theory.

KD	*Energy* (cm^{-1})		g_x	g_y	g_z	ϑ (°)
1	0.000	(0.000)	0.005	0.011	19.043	-
2	92.492	(93.564)	0.042	0.105	15.568	2.392
3	162.238	(163.634)	1.698	1.753	12.530	16.816
4	199.668	(200.414)	8.535	6.595	4.121	114.481
5	226.694	(229.156)	0.491	3.218	12.403	91.735
6	257.712	(261.844)	0.804	1.144	17.833	80.715
7	311.948	(317.667)	0.105	0.285	19.116	105.126
8	493.985	(502.509)	0.000	0.001	19.838	130.083

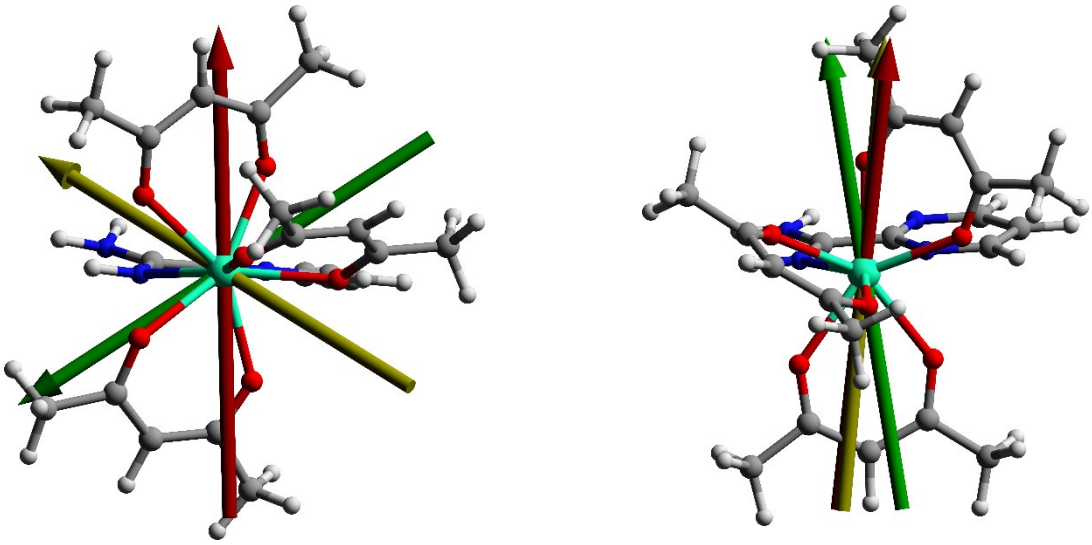

Figure S28. Orientation of the main magnetic axis of the ground (red), first- (yellow) and second-excited (green) KDs in **1** (left) and **2** (right).

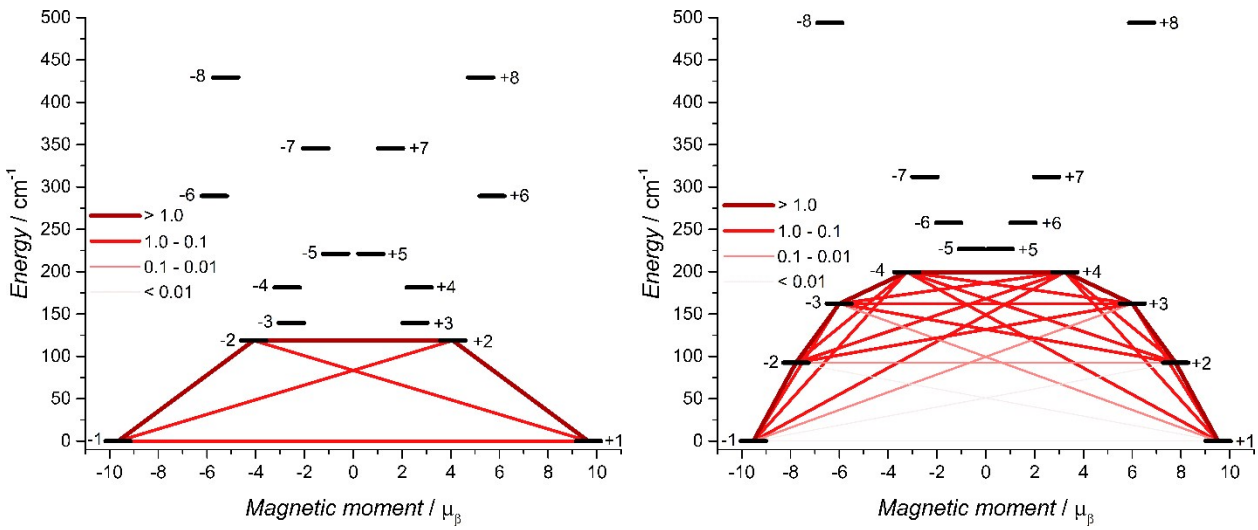

Figure S29. Calculated qualitative energy barrier for **1** (left) and **2** (right). Red lines show the average transition magnetic moment matrix element, that is the transition probabilities, between the respective states. The approximate scale for the transition probabilities is given in Figures and highlighted with different shades of red.

Table S26: Calculated *ab initio* crystal-field parameters B_{kq} (cm^{-1}) presented in the Iwahara–Chibotaru notation for **1**.

k	q	Re|B_{kq}|	Im|B_{kq}|	|B_{kq}|
2	0	-96.37712	0.00000	96.37712
2	1	-35.27120	12.56011	37.44081
2	2	71.20019	-10.55417	71.97817
4	0	-80.64780	0.00000	80.64780
4	1	-0.18241	7.21101	7.21332
4	2	5.70880	-85.29132	85.48216
4	3	-11.16695	10.26142	15.16566
4	4	5.85410	14.16010	15.32249
6	0	-12.05654	0.00000	12.05654
6	1	4.51449	-3.32628	5.60757
6	2	1.79797	1.19710	2.16004
6	3	2.30566	7.92387	8.25251
6	4	-14.59643	-3.42638	14.99320
6	5	-2.71226	1.38251	3.04429
6	6	2.38633	7.34501	7.72294
8	0	0.60076	0.00000	0.60076
8	1	0.09863	-0.05854	0.11470
8	2	-0.21926	0.37374	0.43331
8	3	-0.04714	0.04792	0.06722
8	4	0.00155	-0.06943	0.06945
8	5	0.03332	0.00641	0.03393
8	6	-0.04847	0.10557	0.11616

8	7	0.01158	-0.00175	0.01171
8	8	-0.02079	0.02604	0.03332
10	0	0.02282	0.00000	0.02282
10	1	-0.04737	0.02954	0.05582
10	2	-0.00107	0.00820	0.00827
10	3	0.00144	-0.03000	0.03003
10	4	0.02261	0.01059	0.02497
10	5	0.01644	-0.00390	0.01690
10	6	-0.00969	0.01718	0.01972
10	7	0.00631	0.00489	0.00798
10	8	0.00317	-0.00782	0.00844
10	9	-0.00546	-0.00095	0.00554
10	10	-0.00363	0.00079	0.00371
12	0	-0.00036	0.00000	0.00036
12	1	-0.00008	-0.00012	0.00014
12	2	0.00002	-0.00062	0.00062
12	3	0.00029	0.00004	0.00029
12	4	0.00064	0.00017	0.00067
12	5	0.00036	-0.00014	0.00038
12	6	-0.00017	-0.00020	0.00026
12	7	-0.00011	-0.00046	0.00048
12	8	0.00033	0.00018	0.00037
12	9	0.00013	0.00001	0.00013
12	10	-0.00003	-0.00031	0.00031
12	11	-0.00008	-0.00007	0.00011
12	12	-0.00016	0.00014	0.00021
14	0	-0.00001	0.00000	0.00001
14	1	0.00000	0.00000	0.00000
14	2	0.00000	0.00000	0.00001
14	3	0.00000	0.00000	0.00000
14	4	-0.00001	0.00000	0.00001
14	5	0.00000	0.00000	0.00000
14	6	0.00000	0.00000	0.00000
14	7	0.00000	0.00000	0.00000
14	8	0.00000	0.00000	0.00000
14	9	0.00000	0.00000	0.00000
14	10	0.00000	0.00000	0.00000
14	11	0.00000	0.00000	0.00000
14	12	0.00000	0.00000	0.00000
14	13	0.00000	0.00000	0.00000
14	14	0.00000	0.00000	0.00000

Table S27: Calculated *ab initio* crystal-field parameters B_{kq} (cm^{-1}) presented in the Iwahara–Chibotaru notation for **2**.

k	q	Re|B_{kq}|	Im|B_{kq}|	|B_{kq}|
2	0	-117.99678	0.00000	117.99678
2	1	-58.29463	-29.81924	65.47863
2	2	52.94450	39.76709	66.21587
4	0	-58.51905	0.00000	58.51905
4	1	-27.58199	-0.08862	27.58213
4	2	47.09392	58.95411	75.45479
4	3	-19.87884	-45.95999	50.07484
4	4	15.79152	3.57440	16.19100
6	0	-3.06790	0.00000	3.06790
6	1	17.03179	2.14993	17.16695
6	2	1.97549	2.77907	3.40966
6	3	-4.74498	-7.57015	8.93432
6	4	3.01331	10.61763	11.03695
6	5	9.03492	-4.29633	10.00441
6	6	2.15023	1.99414	2.93259
8	0	0.56072	0.00000	0.56072
8	1	-0.06233	0.08912	0.10875
8	2	-0.33683	-0.29096	0.44509
8	3	0.04772	0.05582	0.07344
8	4	-0.04518	0.00607	0.04558
8	5	0.04892	-0.07249	0.08745
8	6	-0.01548	0.05311	0.05532
8	7	0.04355	-0.00813	0.04430
8	8	-0.01762	-0.03715	0.04112
10	0	0.08456	0.00000	0.08456
10	1	-0.08573	-0.04841	0.09845
10	2	-0.00126	0.00913	0.00922
10	3	0.00974	0.01299	0.01624
10	4	0.00034	0.00235	0.00237
10	5	-0.00373	-0.00589	0.00698
10	6	-0.01013	0.01758	0.02029
10	7	0.02069	-0.00192	0.02078
10	8	-0.00812	-0.00318	0.00872
10	9	0.00446	-0.00587	0.00737
10	10	-0.00010	0.00302	0.00302
12	0	-0.00438	0.00000	0.00438
12	1	-0.00096	-0.00058	0.00112
12	2	0.00139	0.00107	0.00175
12	3	-0.00025	-0.00135	0.00138
12	4	-0.00074	0.00058	0.00094
12	5	-0.00025	-0.00049	0.00056
12	6	-0.00056	0.00034	0.00066

12	7	0.00009	-0.00031	0.00032
12	8	-0.00035	0.00001	0.00035
12	9	0.00025	0.00027	0.00037
12	10	0.00011	-0.00008	0.00014
12	11	0.00014	0.00005	0.00015
12	12	0.00002	0.00002	0.00003
14	0	-0.00003	0.00000	0.00003
14	1	0.00001	0.00001	0.00001
14	2	0.00000	0.00000	0.00000
14	3	0.00001	0.00001	0.00001
14	4	0.00001	-0.00001	0.00001
14	5	0.00001	0.00000	0.00001
14	6	0.00000	0.00000	0.00000
14	7	0.00000	0.00000	0.00000
14	8	0.00000	0.00000	0.00000
14	9	0.00000	0.00000	0.00000
14	10	0.00000	0.00000	0.00000
14	11	0.00000	0.00000	0.00000
14	12	0.00000	0.00000	0.00000
14	13	0.00000	0.00000	0.00000
14	14	0.00000	0.00000	0.00000

XYZ coordinates for PyAm optimized at the PBE1PBE-D3 level of theory

C	-1.78428	-1.14691	-0.30539
H	-2.27857	-2.07917	-0.56472
C	-2.53266	-0.01324	-0.01674
H	-3.61516	-0.05082	-0.04023
C	-1.85649	1.15350	0.29884
H	-2.39771	2.06218	0.53775
C	-0.47128	1.13626	0.31074
H	0.10058	2.02079	0.56435
C	0.18481	-0.05743	0.01784
C	1.68011	-0.11700	0.05318
N	-0.45781	-1.18094	-0.29064
N	2.24821	-1.05534	0.69219
H	3.26406	-0.98407	0.63061
N	2.28560	0.95361	-0.57720
H	3.28345	0.90078	-0.70456
H	1.79008	1.37794	-1.34450

XYZ coordinates for PmAm optimized at the PBE1PBE-D3 level of theory

C	-1.82007	-1.14813	-0.05263
H	-2.35911	-2.09074	-0.09916
C	-2.49724	0.06142	0.00968
H	-3.57832	0.11290	0.01662
C	-1.71117	1.19777	0.05926
H	-2.15025	2.19022	0.10650
C	0.16351	-0.07918	-0.00607
C	1.66644	-0.12471	0.00381
N	-0.49789	-1.22915	-0.06101
N	2.24770	-1.25173	0.11339
H	3.26093	-1.13928	0.10595
N	2.23342	1.11039	-0.14168
H	3.20700	1.22383	0.07735
H	1.62171	1.90298	-0.02277
N	-0.38477	1.13578	0.05091

XYZ coordinates for 1 optimized at the PBE1PBE-D3 level of theory

Dy	-0.15754	0.33843	-0.01040
C	3.49336	2.30298	-2.20872
H	4.22375	1.61131	-1.78089
H	3.94051	3.29309	-2.29633
H	3.24090	1.92931	-3.20418
C	2.25171	2.29511	-1.35610
C	1.80438	3.49967	-0.79873
H	2.36670	4.40084	-1.00298
C	0.64668	3.60059	-0.01546
C	0.22792	4.95114	0.50006
H	-0.76527	5.18452	0.10830
H	0.92244	5.74395	0.22237
H	0.13906	4.90563	1.58814
C	-1.09068	-2.13040	-3.86013
H	-0.68271	-3.04637	-3.42259
H	-0.32716	-1.71492	-4.52206
H	-1.97768	-2.38093	-4.44151
C	-1.37388	-1.14646	-2.75486
C	-2.69771	-0.75041	-2.53201
H	-3.46778	-1.16796	-3.16670
C	-3.07581	0.20481	-1.57727
C	-4.52519	0.58783	-1.45971
H	-4.87159	0.31928	-0.45799
H	-5.15468	0.10027	-2.20392
H	-4.61674	1.67227	-1.55332
C	-2.69035	-3.42953	0.79497

H	-2.94034	-3.45366	-0.26932
H	-3.57481	-3.68456	1.37868
H	-1.91209	-4.17798	0.96211
C	-2.14511	-2.06508	1.12219
C	-2.84006	-1.25799	2.03057
H	-3.74688	-1.65193	2.46996
C	-2.39193	0.00322	2.45815
C	-3.18615	0.73262	3.51035
H	-2.53111	0.98257	4.34861
H	-4.03837	0.15856	3.87412
H	-3.53794	1.67649	3.08604
C	2.15079	-2.07814	-1.09284
H	1.45112	-1.96574	-1.91465
C	3.29087	-2.86723	-1.17857
H	3.50173	-3.41585	-2.08808
C	4.14761	-2.91682	-0.09400
H	5.05774	-3.50446	-0.13205
C	3.83253	-2.18883	1.04430
H	4.50674	-2.17459	1.89172
C	2.66126	-1.44395	1.04976
C	2.22909	-0.61596	2.21016
N	1.84442	-1.38935	-0.00204
N	1.37428	0.30036	1.97729
H	1.03965	0.80946	2.78927
N	2.81689	-0.88630	3.41050
H	2.44680	-0.42225	4.22337
H	3.16637	-1.81517	3.57265
O	1.68772	1.17953	-1.20931
O	-0.09538	2.63408	0.29806
O	-0.37419	-0.74530	-2.10048
O	-2.28443	0.78508	-0.78986
O	-1.07486	-1.74358	0.53757
O	-1.36205	0.58472	2.03584

XYZ coordinates for 2 optimized at the PBE1PBE-D3 level of theory

Dy	0.32161	-0.11328	0.00556
C	0.13244	3.70339	2.71928
H	-0.91588	3.96331	2.54864
H	0.70973	4.61751	2.85677
H	0.17309	3.10550	3.63299
C	0.62525	2.86754	1.56763
C	1.69584	3.33846	0.79932
H	2.14760	4.28195	1.07449
C	2.18956	2.66908	-0.32946
C	3.31834	3.28949	-1.10844
H	4.14691	2.57838	-1.15322
H	3.66565	4.22778	-0.67623

H	2.98881	3.46433	-2.13589
C	4.36456	-1.23616	1.95014
H	4.48337	-0.23529	2.37333
H	5.33560	-1.60892	1.62462
H	3.97357	-1.87601	2.74464
C	3.35894	-1.17266	0.83281
C	3.75461	-1.52824	-0.46162
H	4.77879	-1.84318	-0.61059
C	2.89745	-1.53318	-1.57225
C	3.45137	-1.96019	-2.90645
H	2.82043	-2.75097	-3.31865
H	4.48192	-2.30922	-2.84476
H	3.40224	-1.11178	-3.59469
C	-1.63224	-2.11694	3.78007
H	-0.67683	-2.20107	4.30383
H	-2.24619	-2.98917	4.00399
H	-2.12377	-1.21734	4.15963
C	-1.36139	-1.95427	2.30696
C	-1.86816	-2.91116	1.41702
H	-2.44520	-3.73230	1.82074
C	-1.64647	-2.87315	0.03291
C	-2.24211	-3.95569	-0.82916
H	-2.87532	-3.49654	-1.59259
H	-2.82642	-4.67767	-0.25887
H	-1.43427	-4.47354	-1.35195
C	-2.92672	0.93944	0.95257
H	-2.42238	0.81104	1.90416
C	-4.26335	1.28957	0.83485
H	-4.88348	1.44898	1.70693
C	-4.76720	1.42111	-0.44704
H	-5.80559	1.68449	-0.62317
C	-2.74595	0.90899	-1.30811
C	-1.85350	0.71666	-2.49233
N	-2.17419	0.74197	-0.12281
N	-0.62604	0.47011	-2.24649
H	-0.03082	0.31867	-3.05368
N	-2.47397	0.83391	-3.68013
H	-1.97258	0.73968	-4.54394
H	-3.45455	1.06385	-3.68199
N	-4.01160	1.23666	-1.52716
O	0.01446	1.78318	1.37086
O	1.75310	1.57239	-0.76177
O	2.19994	-0.79426	1.15346
O	1.68247	-1.20896	-1.55555
O	-0.69030	-0.94366	1.97376
O	-0.97315	-1.99581	-0.56547

Luminescent Studies:

The photoluminescence data was obtained using a QuantaMaster 8075-21 Spectrofluorometer (Horiba). An ozone-free PowerArc energy 75 watt Xenon lamp was used as the radiation source. The excitation spectra were corrected in real time according to the lamp intensity and the optical system of the excitation monochromator using a silicon diode as a reference. The emission spectra were corrected according to the optical system of the emission monochromator and the photomultiplier response (Hamamatsu R13456 red extended PMT). Absolute quantum yields were obtained with a K SPHERE Petite integrating sphere. Temperature-dependent measurements were performed with the samples mounted inside a closed cycle helium cryostat system CS202*E-DMX-1AL (Advanced Research Systems) controlled via a LakeShore 335 temperature controller.

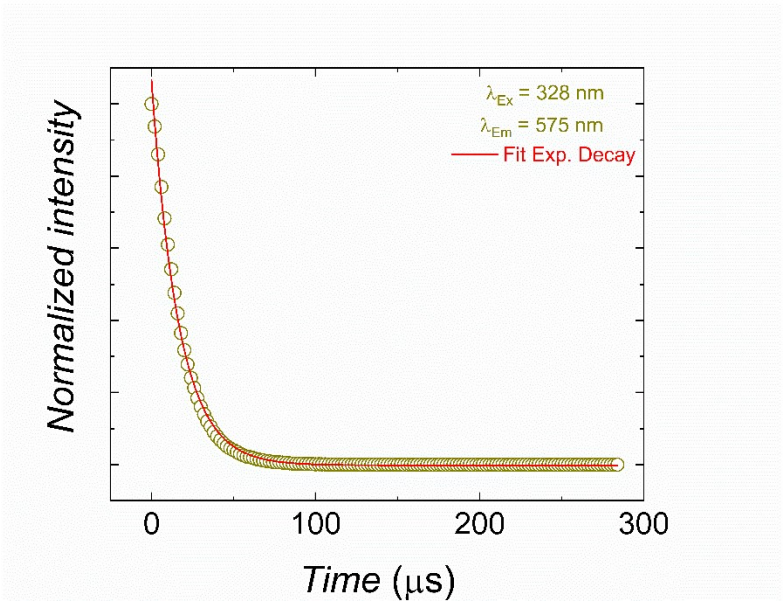

Figure S30. $^4F_{9/2}$ emitter level decay curve for **2** at RT.

Table S28: Emission lifetime and quantum yield (Q_L^{Ln}) of the emitter levels at room temperature for compounds **1** and **2**.

Compound	τ_{RT} / μs	Q_L^{Ln} / %	*Ref*
1	17.8 ± 0.2	8.0 ± 0.5	3
2	16.6 ± 0.5	7.7 ± 0.6	This work

Thermometry:

The thermometric parameter (Δ) chosen for compound **2** is the ratio between I_2 (584-584.5 nm) and I_1 (557-573 nm) (Figure 4C), and the temperature dependence of Δ can be fit as a sigmoidal Logistic function (Eq. 1):

$$\Delta = \frac{A_1 - A_2}{1 + \left({}^{x}/_{x_0} \right)^p} - A_2 \qquad \text{(Eq. S1)}$$

Best-fitting parameters are shown in Figure S31 caption. The thermal relative sensitivity was obtained via Eq. 2:

$$S_r = [(\partial\Delta/\partial T)/\Delta] * 100 \qquad \text{(Eq. S2)}$$

Where the first term is the derivative of the function and the second term is the fitted Δ values.

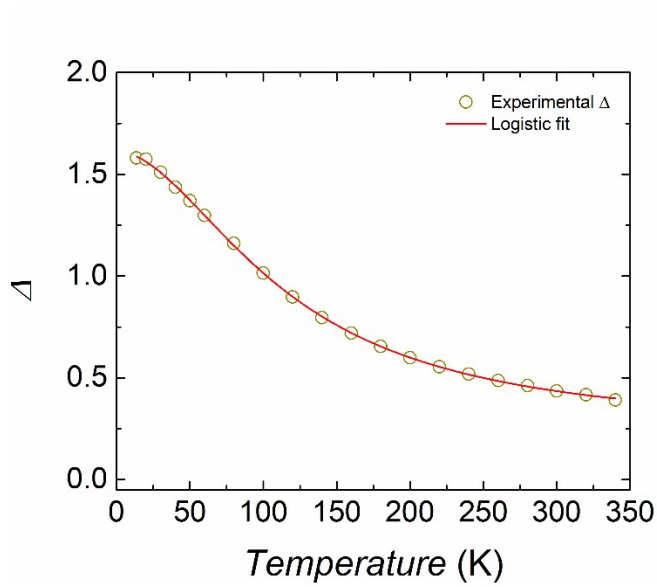

Figure S31. Temperature dependence of the thermometric parameter (*Δ*) for compound **2**, and the Logistic function fitting. Best-fitting parameters: r^2 = 0.999, A_1 = 1.61297, A_2 = 0.23561, x_0 = 115.32547, and p = 1.86144.

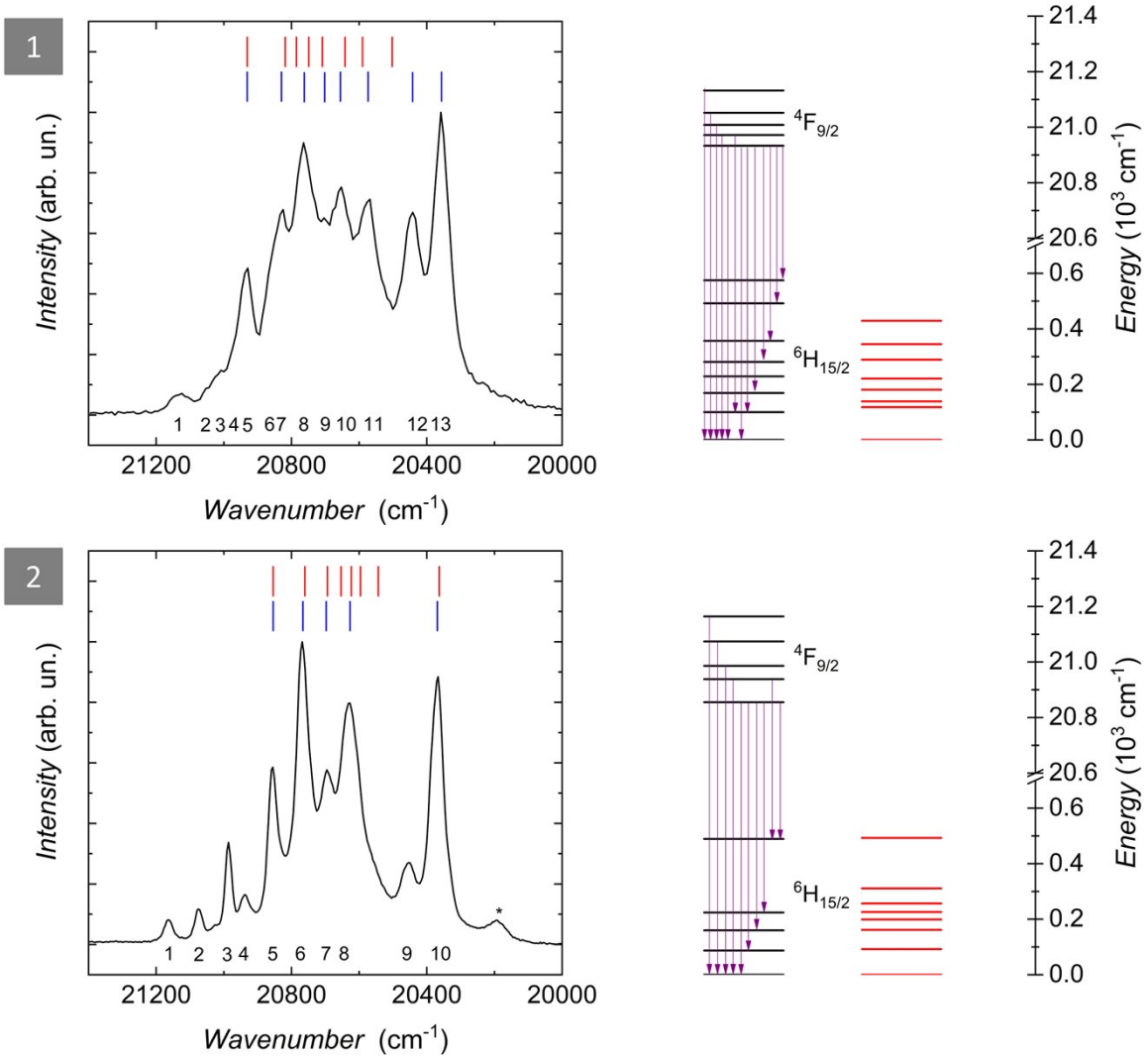

Figure S32. (Left) High-resolution emission spectra ($^4F_{9/2}$→$^6H_{15/2}$) transition band for **1** and **2** obtained at 12 K (λ_{ex}= 325 nm). Blue and red vertical lines refer to the experimental and theoretical levels, respectively. Numbering refer to the observed transitions. * is due to a vibronic side band. (Right) Semi-quantitative partial energy level diagram. Purple arrows refer to the observed transitions and follow the same order than the numbering on the spectra.

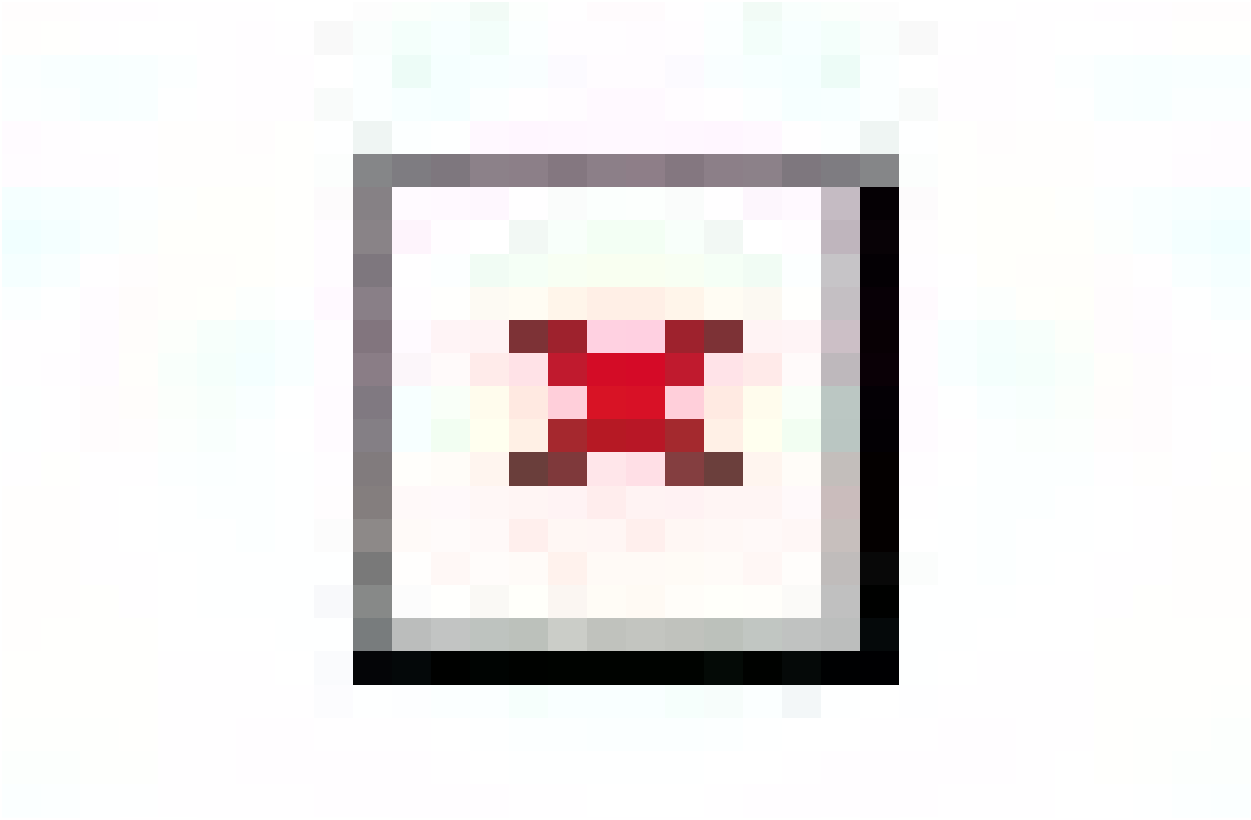

Figure S33. Comparison of the excited state ($^4F_{9/2}$) energy levels for **1** and **2**.

References:

1. A. A. Leitch, I. Korobkov, A. Assoud and J. L. Brusso, *Chem. Commun.*, 2014, **50**, 4934–4936.
2. D. A. Safin, N. A. Tumanov, A. A. Leitch, J. L. Brusso, Y. Filinchuk and M. Murugesu, *CrystEngComm*, 2015, **17**, 2190–2195.
3. A. A. Kitos, D. A. Gálico, R. Castañeda, J. S. Ovens, M. Murugesu and J. L. Brusso, *Inorg. Chem.*, 2020, **59**, 11061–11070.
4. G. M. Sheldrick, SADABS, *Bruker/Siemens Area Detector Absorption Correction Program V.2.0.3*, Bruker AXS: Madison, WI, 2003.
5. G. M. Sheldrick, *Acta Crystallogr. Sect. A: Found. Adv.*, 2015, **71**, 3.
6. G. M. Sheldrick, *SHELXL 2018/3: Programme for Crystal structure refinement, Acta Crystallogr. Sect. C.*, 2015, C**71**, 3.
7. M. Llunell, D. Casanova, J. Girera, P. Alemany and S. Alvarez, *SHAPE V. 2.1*, Barcelona, Spain, 2019.
8. A. L. Spek, *Acta Crystallogr*., 1990, A**46**, C34.
9. M.A. Spackman and D. Jayatilaka, *CrystEngComm*, 2009, **11** ,19-32.
10. L. J. Farrugia, *J. Appl. Crystallogr*., 1999, **32**, 837.
11. K. Brandenburg, *DIAMOND: Program for Crystal and Molecular Structure Visualization*, Crystal Impact GbR, Bonn, Germany, 2014.
12. C. F. Macrae, P. R. Edgington, P. McCabe, E. Pidcock, G. P. Shields, R. Taylor, M. Towler and J. van de Streek, *J. Appl. Crystallogr.*, 2006, **39**, 453.
13. K. Nakamoto, *Infrared and Raman Spectra of Inorganic and Coordination Compounds*, fourth ed., Wiley, New York, 1986, pp. 227-231, 259-263.
14. M. Ernzerhof and G. E. Scuseria, *J. Chem. Phys.*, 1999, **110**, 5029–5036.
15. C. Adamo and V. Barone, *J. Chem. Phys.*, 1999, **110**, 6158–6170.
16. A. Schäfer, C. Huber and R. Ahlrichs, *J. Chem. Phys.*, 1994, **100**, 5829–5835.
17. K. Eichkorn, F. Weigend, O. Treutler and R. Ahlrichs, *Theor. Chem. Acc.*, 1997, **97**, 119–124.
18. T. R. Cundari and W. J. Stevens, *J. Chem. Phys.*, 1993, **98**, 5555–5565.
19. D. Andrae, U. Häußermann, M. Dolg, H. Stoll and H. Preuß, *Theor. Chim. Acta*, 1990, **77**, 123–141.
20. S. Grimme, J. Antony, S. Ehrlich and H. Krieg, *J. Chem. Phys.*, 2010, **132**, 154104.
21. S. Grimme, S. Ehrlich and L. Goerigk, *J. Comput. Chem.*, 2011, **32**, 1456–1465.
22. R.F.W. Bader, *Atoms in Molecules: A Quantum Theory*", Oxford University Press, Oxford (1990)
23. S. Noury, X. Krokidis, F. Fuster and B. Silvi, *Comput. Chem.*, 1999, **23**, 597–604.
24. Gaussian 16, Revision C.01, M. J. Frisch, G. W. Trucks, H. B. Schlegel, G. E. Scuseria, M. A. Robb, J. R. Cheeseman, G. Scalmani, V. Barone, G. A. Petersson, H. Nakatsuji, X. Li, M. Caricato, A. V. Marenich, J. Bloino, B. G. Janesko, R. Gomperts, B. Mennucci, H. P. Hratchian, J. V. Ortiz, A. F. Izmaylov, J. L. Sonnenberg, D. Williams-Young, F. Ding, F. Lipparini, F. Egidi, J. Goings, B. Peng, A. Petrone, T. Henderson, D. Ranasinghe, V. G. Zakrzewski, J. Gao, N. Rega, G. Zheng, W. Liang, M. Hada, M. Ehara, K. Toyota, R. Fukuda, J. Hasegawa, M. Ishida, T. Nakajima, Y. Honda, O. Kitao, H. Nakai, T. Vreven, K. Throssell, J. A. Montgomery, Jr., J. E. Peralta, F. Ogliaro, M. J. Bearpark, J. J. Heyd, E. N. Brothers, K. N. Kudin, V. N. Staroverov, T. A. Keith, R. Kobayashi, J. Normand, K. Raghavachari, A. P. Rendell, J. C. Burant, S. S. Iyengar, J. Tomasi, M. Cossi, J. M. Millam, M. Klene, C. Adamo, R. Cammi, J. W. Ochterski,

R. L. Martin, K. Morokuma, O. Farkas, J. B. Foresman, and D. J. Fox, Gaussian, Inc., Wallingford CT, 2016.
25. AIMAll (Version 19.10.12), Todd A. Keith, TK Gristmill Software, Overland Park KS, USA, 2019.
26. S. Noury, X. Krokidis, F. Fuster and B. Silvi, TopMod package, 1997.
27. D. V. Oliveira, J. Laun, M. F. Peintinger and T. Bredow, *J. Comput. Chem.*, 2019, **40**, 2364–2376.
28. J. Laun, D. V. Oliveira and T. Bredow, *J. Comput. Chem.*, 2018, **39**, 1285–1290.
29. R. Dovesi, A. Erba, R. Orlando, C. M. Zicovich-Wilson, B. Civalleri, L. Maschio, M. Rérat, S. Casassa, J. Baima, S. Salustro and B. Kirtman, *WIREs Comput. Mol. Sci.*, 2018, **8**, e1360.
30. R. Dovesi, V. R. Saunders, C. Roetti, R. Orlando, C. M. Zicovich-Wilson, F. Pascale, B. Civalleri, K. Doll, N. M. Harrison, I. J. Bush, P. D'Arco, M. Llunell, M. Causà, Y. Noël, L. Maschio, A. Erba, M. Rérat and S. Casassa, CRYSTAL17 User's Manual (University of Torino, Torino, 2017).
31. B. O. Roos, P. R. Taylor and P. E. M. Sigbahn, *Chem. Phys.*, 1980, **48**, 157–173.
32. P. Siegbahn, A. Heiberg, B. Roos and B. Levy, *Phys. Scr.*, 1980, **21**, 323–327.
33. B. O. Roos, R. Lindh, P. Å. Malmqvist, V. Veryazov, P.-O. Widmark, *Multiconfigurational Quantum Chemistry*, John Wiley & Sons, Ltd, 1st edn., 2016.
34. B. A. Hess, *Phys. Rev. A*, 1986, **33**, 3742–3748.
35. M. Douglas and N. M. Kroll, *Ann. Phys.*, 1974, **82**, 89–155.
36. B. A. Heß, C. M. Marian, U. Wahlgren and O. Gropen, *Chem. Phys. Lett.*, 1996, **251**, 365–371.
37. B. O. Roos, R. Lindh, P.-Å. Malmqvist, V. Veryazov, P.-O. Widmark and A. C. Borin, *J. Phys. Chem. A*, 2008, **112**, 11431–11435.
38. B. O. Roos, R. Lindh, P.-Å. Malmqvist, V. Veryazov and P.-O. Widmark, *J. Phys. Chem. A*, 2004, **108**, 2851–2858.
39. D. Peng and M. Reiher, *Theor. Chem. Acc.*, 2012, **131**, 1081.
40. M. Filatov, *J. Chem. Phys.*, 2006, **125**, 107101.
41. W. Kutzelnigg and W. Liu, *J. Chem. Phys.*, 2005, **123**, 241102.
42. A. A. Granovsky, *J. Chem. Phys.*, 2011, **134**, 214113.
43. T. Shiozaki, W. Győrffy, P. Celani and H.-J. Werner, *J. Chem. Phys.*, 2011, **135**, 081106.
44. L. Ungur, W. V. den Heuvel and L. F. Chibotaru, *New J. Chem.*, 2009, **33**, 1224–1230.
45. L. F. Chibotaru, L. Ungur and A. Soncini, *Angew. Chem. Int. Ed.*, 2008, **47**, 4126–4129.
46. N. Ishikawa, M. Sugita and W. Wernsdorfer, *Angew. Chem. Int. Ed.*, 2005, **44**, 2931-2935.
47. F. Habib, P.-H. Lin, J. Long, I. Korobkov, W. Wernsdorfer and M. Murugesu, *J. Am. Chem. Soc.*, 2011, **133**, 8830-8833.
48. I. Fdez. Galván, M. Vacher, A. Alavi, C. Angeli, F. Aquilante, J. Autschbach, J. J. Bao, S. I. Bokarev, N. A. Bogdanov, R. K. Carlson, L. F. Chibotaru, J. Creutzberg, N. Dattani, M. G. Delcey, S. S. Dong, A. Dreuw, L. Freitag, L. M. Frutos, L. Gagliardi, F. Gendron, A. Giussani, L. González, G. Grell, M. Guo, C. E. Hoyer, M. Johansson, S. Keller, S. Knecht, G. Kovačević, E. Källman, G. Li Manni, M. Lundberg, Y. Ma, S. Mai, J. P. Malhado, P. Å. Malmqvist, P. Marquetand, S. A. Mewes, J. Norell, M. Olivucci, M. Oppel, Q. M. Phung, K. Pierloot, F. Plasser, M. Reiher, A. M. Sand, I. Schapiro, P. Sharma, C. J. Stein, L. K. Sørensen, D. G. Truhlar, M. Ugandi, L. Ungur, A. Valentini, S. Vancoillie, V. Veryazov, O. Weser, T. A. Wesołowski, P.-O. Widmark, S. Wouters, A. Zech, J. P. Zobel and R. Lindh, *J. Chem. Theory Comput.*, 2019, **15**, 5925–5964.
49. L. Ungur, M. Thewissen, J.-P. Costes, W. Wernsdorfer and L. F. Chibotaru, *Inorg. Chem.*, 2013, **52**, 6328–6337.

50. L. Ungur and L. F. Chibotaru, *Chem. – Eur. J.*, 2017, **23**, 3708–3718.
51. L. F. Chibotaru and L. Ungur, *J. Chem. Phys.*, 2012, **137**, 064112.
52. D. Reta and N. F. Chilton, *Phys. Chem. Chem. Phys.*, 2019, **21**, 23567-23575.
53. D. Errulat, R. Marin, D. A. Gálico, K. L. M. Harriman, A. Pialat, B. Gabidullin, F. Iikawa, O. D. D. Couto Jr., J. O. Moilanen, E. Hemmer, F. A. Sigoli and M. Murugesu, *ACS Cent. Sci.*, 2019, **5**, 1187-1198.
54. K. L. M. Harriman, D. Errula and M. Murugesu, *Trends in Chemistry*, 2019, **1**.